Discrete-Fourier-Transform-Based Framework for Analysis and Synthesis of Cylindrical Omega-Bianisotropic Metasurfaces

Gengyu Xu,* George V. Eleftheriades, and Sean V. Hum
The Edward S. Rogers Sr. Department of Electrical and Computer Engineering, University of Toronto, Toronto, Ontario M5S 3H7, Canada

(Received 20 July 2020; revised 5 October 2020; accepted 12 November 2020; published 17 December 2020)

This paper presents a framework for analyzing and designing cylindrical omega-bianisotropic metasurfaces, inspired by mode matching and digital signal-processing techniques. Using the discrete Fourier transform, we decompose the electromagnetic field distributions into orthogonal cylindrical modes and convert the azimuthally varying metasurface constituent parameters into their respective spectra. Then, by invoking appropriate boundary conditions, we set up systems of algebraic equations, which can be rearranged to either predict the scattered fields of prespecified metasurfaces, or to synthesize metasurfaces, which support arbitrarily stipulated field transformations. The proposed framework facilitates the efficient evaluation of field distributions that satisfy local power conservation, which is one of the key difficulties involved with the design of passive and lossless scalar metasurfaces. It represents a promising solution to circumvent the need for active components, controlled power dissipation, or tensorial surface polarizabilities in many state-of-the-art conformal metasurface-based devices. To demonstrate the robustness and the versatility of the proposed technique, we design several devices intended for different applications and numerically verify them using finite-element simulations.

DOI: 10.1103/PhysRevApplied.14.064055

I. INTRODUCTION

Electromagnetic metasurfaces are devices of subwavelength thickness consisting of two-dimensional arrangements of scatterers (meta-atoms) with engineered electric and/or magnetic polarizabilities and subwavelength dimensions [1,2]. Due to their extraordinary ability to efficiently manipulate various aspects of electromagnetic waves, metasurfaces have been leveraged in a variety of practical applications. For example, beam redirectors and splitters [3–7], flat lenses [8], frequency filters [9, 10], polarization transformers [11,12], and electromagnetic cloaks [13–16] have all been successfully demonstrated. Of the various reported metasurface-based devices, those exhibiting omega-bianisotropy have been particularly fascinating, due to their abilities to realize highly sophisticated field transformations with near-perfect efficiencies [17–19]. Their robustness stems from the cross-coupling between the electric and magnetic responses, which represents an additional degree of freedom that can be engineered at will.

Much of the research efforts so far in the area of metasurfaces have been devoted to flat planar surfaces. However recently, cylindrical metasurfaces have also generated significant interests due to the potential applications offered by their unique geometries. For instance, the fact that they can completely enclose an object make them ideal for electromagnetic interference reduction and cloaking [13–16]. They have also been used to create electromagnetic illusions [20,21] and conformal antennas [22].

Wave scattering by cylindrical metasurfaces can be accurately predicted using integral equations based on tensorial bianisotropic sheet transition conditions (BSTCs) [23,24]. Alternatively, one can analyze these surfaces using mode matching [25]. While the latter technique is more suitable for impedance surfaces, it is possible to generalize it for omega-bianisotropic metasurfaces since they can be constructed from multiple concentric impedance surfaces. By cascading the generalized scattering matrices (GSMs) of its constituent layers, a multilayer omega-bianisotropic metasurface (OBMS) can be accurately modeled [26].

Although these approaches provide accurate predictions for the scattered fields of a cylindrical metasurface, they are inherently analysis techniques, which do not offer any insights on how to synthesize a surface to perform the desired field transformations. For instance, the cascaded GSMs of impedance surfaces is essentially a black box that does not reveal how its components should be engineered.

While it is possible to synthesize a cylindrical OBMS by specifying the desired fields everywhere and solving the BSTC equations to obtain the required surface

*paul.xu@mail.utoronto.ca

parameters, the resulting designs will be generally active and/or lossy. These designs are usually undesirable as they require active components and/or accurately controlled Ohmic losses to implement in practice. A technique to identify field distributions that correspond to passive and lossless designs has been reported [16]. However, it is based on numerical optimization of the spatial distribution of electromagnetic fields, which can be difficult.

In this article, we present a mode-matching framework for analysis and synthesis of circular cylindrical OBMSs inspired by concepts in digital signal processing. The fields everywhere are decomposed into cylindrical modes using the discrete Fourier transform, while the bianisotropic parameters of the metasurface is transformed into their respective spectra. Then, by invoking the BSTCs, we set up systems of algebraic equations, which can be easily solved to either model the scattering behavior of complex OBMSs, or to synthesize devices that can perform stipulated field transformations. In contrast with previous mode-matching methods, our formulation inherently accounts for the potentially bianisotropic polarizabilities of the metasurface, without needing to decompose it into several constituent parts. This facilitates the derivation of closed-form synthesis equations. Furthermore, the algebraic formulation simplifies the process of identifying passive and lossless field distributions, leading to very practical metasurface designs.

Using the proposed method, we design and investigate several passive and lossless cylindrical OBMS-based devices. In order to validate the designs, they are each simulated numerically in COMSOL Multiphysics. An electromagnetic illusion metasurface constructed with realistic meta-atoms is designed and verified in Ansys HFSS.

II. THEORY

The concepts presented in this paper can be applied to any scalar circular cylindrical omega-bianisotropic metasurfaces. However, some of the steps throughout the analysis and synthesis require slight problem-specific modifications. In this section, for illustrative purposes, we investigate the case of an internally excited OBMS. Generalization to other configurations are discussed subsequently when they arise.

The problem under consideration is depicted in Fig. 1. The metasurface, characterized by its ϕ-dependent surface electric impedance $Z_{\mathrm{SE}}(\phi)$, surface magnetic admittance $Y_{\mathrm{SM}}(\phi)$, and magnetoelectric coupling coefficient $K_{\mathrm{EM}}(\phi)$, forms a closed cylindrical cavity of radius α. In this paper, we only consider two-dimensional problems, which are invariant in the z direction. For the sake of simplicity, let us assume the fields are transverse magnetic with respect to the z axis (TM^z) with an implicit time dependency of $e^{j\omega t}$. This means we have $\vec{E} = \hat{z}E_z$. Extension

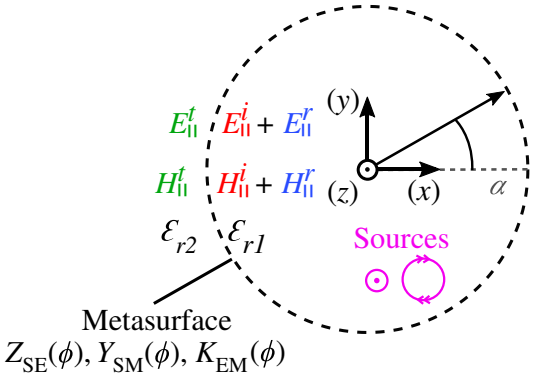

FIG. 1. Geometric configuration of the internally excited circular cylindrical OBMS.

to transverse-electric (TE^z) configurations ($\vec{H} = \hat{z}H_z$) is straightforward, and is not explicated here.

As indicated, the internal and the external regions of the OBMS have relative permittivities ϵ_{r1} and ϵ_{r2}, respectively.

The fields enclosed by the cylinder consist of the incident electric and magnetic fields $\{E^i_{\|}, H^i_{\|}\}$ in addition to the reflected fields $\{E^r_{\|}, H^r_{\|}\}$. The fields external to the cylinder are just the transmitted fields $\{E^t_{\|}, H^t_{\|}\}$. The subscript "$\|$" denotes the transverse components of the fields, which are the components of interest in the present configuration. For TM^z-polarized field distributions, these correspond to the z component of the electric fields and the ϕ component of the magnetic fields.

In accordance with the cylindrical coordinate system, the fields inside and outside of the metasurface cavity can be written as series of cylindrical modes described by

$$
\begin{aligned}
E^i_z(\rho,\phi) &= \sum_{p=-\infty}^{\infty} e^i_p \frac{H^{(2)}_p(k_1\rho)}{H^{(2)}_p(k_1\alpha)} e^{-jp\phi},\\
H^i_\phi(\rho,\phi) &= \sum_{p=-\infty}^{\infty} e^i_p Y^i_{\mathrm{in},p}(\rho) \frac{H^{(2)}_p(k_1\rho)}{H^{(2)}_p(k_1\alpha)} e^{-jp\phi},\\
E^t_z(\rho,\phi) &= \sum_{p=-\infty}^{\infty} e^t_p \frac{H^{(2)}_p(k_2\rho)}{H^{(2)}_p(k_2\alpha)} e^{-jp\phi},\\
H^t_\phi(\rho,\phi) &= \sum_{p=-\infty}^{\infty} e^t_p Y^t_{\mathrm{in},p}(\rho) \frac{H^{(2)}_p(k_2\rho)}{H^{(2)}_p(k_2\alpha)} e^{-jp\phi},\\
E^r_z(\rho,\phi) &= \sum_{p=-\infty}^{\infty} e^r_p \frac{J_p(k_1\rho)}{J_p(k_1\alpha)} e^{-jp\phi},\\
H^r_\phi(\rho,\phi) &= \sum_{p=-\infty}^{\infty} e^r_p Y^r_{\mathrm{in},p}(\rho) \frac{J_p(k_1\rho)}{J_p(k_1\alpha)} e^{-jp\phi},\\
k_{\{1,2\}} &= \sqrt{\epsilon_{r\{1,2\}}}k_o,
\end{aligned}
\tag{1}
$$

where k_o is the free-space wave number. $H_p^{(2)}(\cdot)$ denotes the pth-order Hankel function of second kind and $J_p(\cdot)$ denotes the pth-order Bessel function. The coefficients $e_p^{\{i,t,r\}}$ are the complex amplitudes of the pth mode of the incident, transmitted and reflected electric fields evaluated at $\rho = \alpha$.

The pth modes of $E_z^{\{i,t,r\}}$ can be related to the pth modes of $H_\phi^{\{i,t,r\}}$ by the modal wave admittances $Y_{\text{in},p}^{\{i,t,r\}}(\rho)$, where the subscript "in,p" indicates that these are the pth mode admittances for an internally excited metasurface. As discussed in Sec. III, the fields of the externally excited surface have different modal wave admittances, indicated by their distinct subscripts.

By invoking the linearity of Maxwell's equations and the orthogonality of the cylindrical modal wave functions, the expressions for $Y_{\text{in},p}^{\{i,t,r\}}(\rho)$ are found to be

$$\begin{aligned} Y_{\text{in},p}^{i}(\rho) &= -\frac{j\sqrt{\epsilon_{r1}}}{\eta_o}\frac{H_p^{(2)'}(k_1\rho)}{H_p^{(2)}(k_1\rho)}, \\ Y_{\text{in},p}^{t}(\rho) &= -\frac{j\sqrt{\epsilon_{r2}}}{\eta_o}\frac{H_p^{(2)'}(k_2\rho)}{H_p^{(2)}(k_2\rho)}, \\ Y_{\text{in},p}^{r}(\rho) &= -\frac{j\sqrt{\epsilon_{r1}}}{\eta_o}\frac{J_p'(k_1\rho)}{J_p(k_1\rho)}. \end{aligned} \tag{2}$$

The derivatives in Eq. (2) are evaluated with respect to the entire arguments of $H_p^{(2)}(\cdot)$ and $J_p(\cdot)$.

The exact values of the coefficients $e_p^{\{i,t,r\}}$ can be obtained by performing a Fourier transform on the corresponding fields along a closed circle centered at the origin. In a similar manner, the surface properties $Z_{\text{SE}}(\phi)$, $Y_{\text{SM}}(\phi)$, and $K_{\text{EM}}(\phi)$ can be decomposed into their constituent Fourier harmonics because they are also 2π periodic. This idea forms the basis of our analysis and synthesis methods, described in Sec. II A and Sec. II B, respectively.

A. Analysis of internally excited circular cylindrical omega-bianisotropic metasurfaces

We first present a method for evaluating the scattered fields from internally excited circular cylindrical OBMSs. We begin by discretizing the surface into N equally sized unit cells. The surface properties can be sampled at the centers of these cells, forming $N \times 1$ vectors $\bar{Z}_{\text{SE}}$, $\bar{Y}_{\text{SM}}$, and $\bar{K}_{\text{EM}}$ whose entries are

$$\begin{aligned} \bar{Z}_{\text{SE}}[n] &= Z_{\text{SE}}\big|_{\phi=(n-1)\Delta_\phi}, \\ \bar{Y}_{\text{SM}}[n] &= Y_{\text{SM}}\big|_{\phi=(n-1)\Delta_\phi}, \\ \bar{K}_{\text{EM}}[n] &= K_{\text{EM}}\big|_{\phi=(n-1)\Delta_\phi}, \end{aligned} \tag{3}$$

where $\Delta_\phi = 2\pi/N$ is the azimuthal extent of one unit cell.

We can also sample the tangential fields on the internal and external facets of each unit cell to obtain $N \times 1$ field vectors

$$\begin{aligned} \bar{E}_z^t[n] &= E_z^t\big|_{\rho\to\alpha^+,\phi=(n-1)\Delta_\phi}, \\ \bar{E}_z^{\{i,r\}}[n] &= E_z^{\{i,r\}}|_{\rho\to\alpha^-,\phi=(n-1)\Delta_\phi}, \\ \bar{H}_\phi^t[n] &= H_\phi^t|_{\rho\to\alpha^+,\phi=(n-1)\Delta_\phi}, \\ \bar{H}_\phi^{\{i,r\}}[n] &= H_\phi^{\{i,r\}}|_{\rho\to\alpha^-,\phi=(n-1)\Delta_\phi}. \end{aligned} \tag{4}$$

Alternatively, since all vectors in Eqs. (3) and (4) correspond to quantities that are 2π periodic in ϕ, they can be represented in terms of their N-point discrete Fourier transforms (NDFTs) via multiplications with the NDFT matrix $\mathbf{W}_N$:

$$\begin{aligned} &\hat{E}_z^{\{i,r,t\}} = \mathbf{W}_N\bar{E}_z^{\{i,r,t\}}, \quad \hat{H}_z^{\{i,r,t\}} = \mathbf{W}_N\bar{H}_z^{\{i,r,t\}}, \\ &\hat{Z}_{\text{SE}} = \mathbf{W}_N\bar{Z}_{\text{SE}}, \quad \hat{Y}_{\text{SM}} = \mathbf{W}_N\bar{Y}_{\text{SM}}, \quad \hat{K}_{\text{EM}} = \mathbf{W}_N\bar{K}_{\text{EM}}. \end{aligned} \tag{5}$$

$\mathbf{W}_N$ is the NDFT matrix whose elements are

$$\begin{aligned} \mathbf{W}_N[n][m] &= \frac{1}{N}e^{j\frac{2\pi}{N}n^\star(m-1)}, \\ n^\star &\triangleq n - \frac{N+1}{2}. \end{aligned} \tag{6}$$

We refer to $\hat{E}_z^{\{i,r,t\}}$ and $\hat{H}_\phi^{\{i,r,t\}}$ as the modal field vectors, since their entries represent the amplitudes of the constituent cylindrical modes of $E_z^{\{i,r,t\}}$ and $H_\phi^{\{i,r,t\}}$, evaluated at $\rho = \alpha$. On the other hand, $\hat{Z}_{\text{SE}}$, $\hat{Y}_{\text{SM}}$, and $\hat{K}_{\text{EM}}$ are the surface property spectra whose entries represent the amplitudes of the Fourier harmonics constituting $\bar{Z}_{\text{SE}}$, $\bar{Y}_{\text{SM}}$, and $\bar{K}_{\text{EM}}$.

The rows of $\mathbf{W}_N$, as defined by Eq. (6), are arranged such that the center entries of the modal field vectors and the surface property spectra correspond to the $p = 0$ expansion term. The first and last entries correspond to the $p = (1-N)/2 \triangleq p_-$ and $p = (N-1)/2 \triangleq p_+$ terms, respectively.

One advantage of the modal analysis presented herein is that $\hat{E}_z^{\{i,r,t\}}$ can be algebraically related to $\hat{H}_\phi^{\{i,r,t\}}$ with the help of Eq. (2). More specifically, we can write

$$\begin{aligned} \hat{H}_\phi^{\{i,t,r\}} &= \mathbf{Y}_{\text{in}}^{\{i,t,r\}}\hat{E}_z^{\{i,t,r\}}, \\ \mathbf{Y}_{\text{in}}^{\{i,t,r\}} &= \text{diag}\begin{bmatrix} Y_{\text{in},p_-}^{\{i,t,r\}}(\alpha) & \cdots & Y_{\text{in},p_+}^{\{i,t,r\}}(\alpha) \end{bmatrix}^T, \end{aligned} \tag{7}$$

where $\mathbf{Y}_{\text{in}}^{\{i,t,r\}}$ are the diagonal modal admittance matrices for the incident, transmitted, and reflected fields. They can be used to eliminate all magnetic field quantities from the analysis, thereby reducing the number of unknowns. Due

to the different wave-admittance expressions, other configurations such as externally excited surfaces may require slightly different modal admittance matrices.

The original goal of this section is to predict the transmitted and reflected fields, given the incident fields and the OBMS surface parameters. To this end, we now relate the field vectors on either side of the metasurface by invoking the BSTCs at each of the N unit cells [17]. Doing so results in the system of equations:

$$\begin{aligned}\frac{1}{2}(\bar{E}_z^t+\bar{E}_z^i+\bar{E}_z^r)&=\bar{Z}_{\mathrm{SE}}\odot(\bar{H}_\phi^t-\bar{H}_\phi^i-\bar{H}_\phi^r)\\&\quad-\bar{K}_{\mathrm{EM}}\odot(\bar{E}_z^t-\bar{E}_z^i-\bar{E}_z^r),\\\frac{1}{2}(\bar{H}_\phi^t+\bar{H}_\phi^i+\bar{H}_\phi^r)&=\bar{Y}_{\mathrm{SM}}\odot(\bar{E}_z^t-\bar{E}_z^i-\bar{E}_z^r)\\&\quad+\bar{K}_{\mathrm{EM}}\odot(\bar{H}_\phi^t-\bar{H}_\phi^i-\bar{H}_\phi^r),\end{aligned}\tag{8}$$

where $\odot$ denotes element-wise multiplication.

In order to take advantage of the simplifications offered by modal analysis, we transform Eq. (8) using the circular convolution theorem for NDFT, which says

$$\mathbf{W}_N(\bar{U}\odot\bar{V})=\hat{U}\circledast_N\hat{V}=\hat{\mathbf{U}}\hat{V}.\tag{9}$$

The operation $\circledast_N$ denotes modulo-N circular convolution. As alluded to by the second equality in Eq. (9), we can implement this operation as a matrix multiplication by transforming the first operand $\hat{U}$ into the $N\times N$ circulant matrix $\hat{\mathbf{U}}$ given by

$$\hat{\mathbf{U}}=\mathbf{W}_N\mathrm{diag}(\mathbf{W}_N^{-1}\hat{U})\mathbf{W}_N^{-1}.\tag{10}$$

Applying NDFT to both sides of Eq. (8) and applying Eqs. (7) and (9), we obtain a new system of equations:

$$\begin{aligned}&\frac{1}{2}(\hat{E}_z^t+\hat{E}_z^i+\hat{E}_z^r)\\&=\hat{\mathbf{Z}}(\mathbf{Y}_{\mathrm{in}}^t\hat{E}_z^t-\mathbf{Y}_{\mathrm{in}}^i\hat{E}_z^i-\mathbf{Y}_{\mathrm{in}}^r\hat{E}_z^r)-\hat{\mathbf{K}}(\hat{E}_z^t-\hat{E}_z^i-\hat{E}_z^r),\\&\frac{1}{2}(\mathbf{Y}_{\mathrm{in}}^t\hat{E}_z^t+\mathbf{Y}_{\mathrm{in}}^i\hat{E}_z^i+\mathbf{Y}_{\mathrm{in}}^r\hat{E}_z^r)\\&=\hat{\mathbf{Y}}(\hat{E}_z^t-\hat{E}_z^i-\hat{E}_z^r)+\hat{\mathbf{K}}(\mathbf{Y}_{\mathrm{in}}^t\hat{E}_z^t-\mathbf{Y}_{\mathrm{in}}^i\hat{E}_z^i-\mathbf{Y}_{\mathrm{in}}^r\hat{E}_z^r),\end{aligned}\tag{11}$$

where $\hat{\mathbf{Z}}$, $\hat{\mathbf{Y}}$, and $\hat{\mathbf{K}}$ are $N\times N$ circulant matrices formed by $\hat{Z}_{\mathrm{SE}}$, $\hat{Y}_{\mathrm{SM}}$, and $\hat{K}_{\mathrm{EM}}$, respectively. This set of equations can be easily rearranged to solve for the modal transmission matrix $\hat{\mathbf{T}}_{\mathrm{in}}$ and the modal reflection matrix $\hat{\mathbf{R}}_{\mathrm{in}}$; they relate $\hat{E}_z^t$ and $\hat{E}_z^r$ to $\hat{E}_z^i$ according to

$$\hat{E}_z^t=\hat{\mathbf{T}}_{\mathrm{in}}\hat{E}_z^i,\quad\hat{E}_z^r=\hat{\mathbf{R}}_{\mathrm{in}}\hat{E}_z^i.\tag{12}$$

The exact solutions for the two matrices are

$$\begin{aligned}\hat{\mathbf{T}}_{\mathrm{in}}&=\hat{\mathbf{t}}_{\mathrm{in},b}^{-1}\hat{\mathbf{t}}_{\mathrm{in},a},\\\hat{\mathbf{t}}_{\mathrm{in},a}&=\left(\frac{1}{2}\mathbf{I}-\hat{\mathbf{K}}+\hat{\mathbf{Z}}\mathbf{Y}_{\mathrm{in}}^r\right)^{-1}\left(\frac{1}{2}\mathbf{I}-\hat{\mathbf{K}}+\hat{\mathbf{Z}}\mathbf{Y}_{\mathrm{in}}^i\right)\\&\quad-\left(\frac{1}{2}\mathbf{Y}_{\mathrm{in}}^r+\hat{\mathbf{Y}}+\hat{\mathbf{K}}\mathbf{Y}_{\mathrm{in}}^r\right)^{-1}\left(\frac{1}{2}\mathbf{Y}_{\mathrm{in}}^i+\hat{\mathbf{Y}}+\hat{\mathbf{K}}\mathbf{Y}_{\mathrm{in}}^i\right),\\\hat{\mathbf{t}}_{\mathrm{in},b}&=\left(\frac{1}{2}\mathbf{Y}_{\mathrm{in}}^r+\hat{\mathbf{Y}}+\hat{\mathbf{K}}\mathbf{Y}_{\mathrm{in}}^r\right)^{-1}\left(\frac{1}{2}\mathbf{Y}_{\mathrm{in}}^t-\hat{\mathbf{Y}}-\hat{\mathbf{K}}\mathbf{Y}_{\mathrm{in}}^t\right)\\&\quad-\left(\frac{1}{2}\mathbf{I}-\hat{\mathbf{K}}+\hat{\mathbf{Z}}\mathbf{Y}_{\mathrm{in}}^r\right)^{-1}\left(\frac{1}{2}\mathbf{I}+\hat{\mathbf{K}}-\hat{\mathbf{Z}}\mathbf{Y}_{\mathrm{in}}^t\right),\\\hat{\mathbf{R}}_{\mathrm{in}}&=\hat{\mathbf{r}}_{\mathrm{in},b}^{-1}\hat{\mathbf{r}}_{\mathrm{in},a},\\\hat{\mathbf{r}}_{\mathrm{in},a}&=\left(\frac{1}{2}\mathbf{I}+\hat{\mathbf{K}}-\hat{\mathbf{Z}}\mathbf{Y}_{\mathrm{in}}^t\right)^{-1}\left(\frac{1}{2}\mathbf{I}-\hat{\mathbf{K}}+\hat{\mathbf{Z}}\mathbf{Y}_{\mathrm{in}}^i\right)\\&\quad-\left(\frac{1}{2}\mathbf{Y}_{\mathrm{in}}^t-\hat{\mathbf{Y}}-\hat{\mathbf{K}}\mathbf{Y}_{\mathrm{in}}^t\right)^{-1}\left(\frac{1}{2}\mathbf{Y}_{\mathrm{in}}^i+\hat{\mathbf{Y}}+\hat{\mathbf{K}}\mathbf{Y}_{\mathrm{in}}^i\right),\\\hat{\mathbf{r}}_{\mathrm{in},b}&=\left(\frac{1}{2}\mathbf{Y}_{\mathrm{in}}^t-\hat{\mathbf{Y}}-\hat{\mathbf{K}}\mathbf{Y}_{\mathrm{in}}^t\right)^{-1}\left(\frac{1}{2}\mathbf{Y}_{\mathrm{in}}^r+\hat{\mathbf{Y}}+\hat{\mathbf{K}}\mathbf{Y}_{\mathrm{in}}^r\right)\\&\quad-\left(\frac{1}{2}\mathbf{I}+\hat{\mathbf{K}}-\hat{\mathbf{Z}}\mathbf{Y}_{\mathrm{in}}^t\right)^{-1}\left(\frac{1}{2}\mathbf{I}-\hat{\mathbf{K}}+\hat{\mathbf{Z}}\mathbf{Y}_{\mathrm{in}}^r\right).\end{aligned}\tag{13}$$

Here, $\mathbf{I}$ is the $N\times N$ identity matrix. Since $\hat{H}_\phi^t$ and $\hat{H}_\phi^r$ can be found using Eq. (7), we have completed our analysis.

B. Synthesis of internally excited circular cylindrical omega-bianisotropic metasurfaces

Within the proposed DFT framework, it is also possible to synthesize the required surface properties for realizing a stipulated field transformation.

While the analysis presented in Sec. II A applies to general OBMSs that can contain power gain and/or loss, we devote our effort henceforth to the synthesis of passive and lossless metasurfaces. This is because they are much easier to implement in practice, requiring only reactive components, which can be realized with etched patterns on printed circuit boards (PCBs). Often, the undesirable losses associated with realistic PCBs are not pronounced enough to significantly corrupt the functionalities of a fabricated device, even if losslessness is assumed throughout the entire design process [7].

Previously, it was shown that a sufficient condition for an OBMS to be passive and lossless is that the field transformation being performed satisfies local power conservation (LPC) [17], which can be described by the equation

$$\mathrm{Re}\left\{(\bar{E}_z^i+\bar{E}_z^r)\odot(\bar{H}_\phi^i+\bar{H}_\phi^r)^*\right\}=\mathrm{Re}\left\{\bar{E}_z^t\odot\bar{H}_\phi^{t^*}\right\},\tag{14}$$

where $(\cdot)^*$ denotes complex conjugation. Although composite metasurface systems, which satisfy global power conservation represent possible alternatives [27], they are much harder to design and implement. Thus, we strictly focus on surfaces that satisfy LPC. From Eq. (14), it can be inferred that a passive and lossless transmissive scalar metasurface, which is one that produces a prescribed transmitted field distribution from a known incident field, should generate some amount of parasitic reflected fields (termed "auxiliary reflection"). Similarly, a passive and lossless reflective scalar metasurface requires some auxiliary transmission. Naturally, depending on the type of metasurface to be synthesized, we first need to solve for either $\{\bar{E}^r, \bar{H}^r\}$ or $\{\bar{E}^t, \bar{H}^t\}$. To do this directly using Eq. (14) can be challenging. One needs to solve a system of coupled nonlinear differential equations since the unknown auxiliary electric fields and auxiliary magnetic fields are related through Maxwell's equations. In this work, we use Eq. (7) to eliminate $\bar{H}_\phi^{\{i,t,r\}}$ from the equation, yielding a nonlinear algebraic equation, which can be solved numerically with ease. For transmissive metasurfaces, where $\bar{E}_z^r$ or $\hat{E}_z^r$ is the unknown, we have

$$\begin{aligned}&\mathrm{Re}\{(\bar{E}_z^i + \mathbf{W}_N^{-1}\hat{E}_z^r) \odot (\bar{H}_\phi^i + \mathbf{W}_N^{-1}\mathbf{Y}_{\mathrm{in}}^r\hat{E}_z^r)^*\}\\ &\quad = \mathrm{Re}\{\bar{E}_z^t \odot \bar{H}_\phi^{t^*}\}.\end{aligned} \tag{15}$$

For reflective metasurfaces, where $\bar{E}_z^t$ or $\hat{E}_z^t$ is the unknown, the equation to solve is

$$\begin{aligned}&\mathrm{Re}\{(\bar{E}_z^i + \bar{E}_z^r) \odot (\bar{H}_\phi^i + \bar{E}_z^r)^*\}\\ &\quad = \mathrm{Re}\{(\mathbf{W}_N^{-1}\hat{E}_z^t) \odot (\mathbf{W}_N^{-1}\mathbf{Y}_{\mathrm{in}}^t\hat{E}_z^t)^*\}.\end{aligned} \tag{16}$$

Solving either Eq. (15) or Eq. (16) gives the complete field distributions everywhere. We can proceed by assessing the required $\{\bar{Z}_{\mathrm{SE}}, \bar{Y}_{\mathrm{SM}}, \bar{K}_{\mathrm{EM}}\}$, which supports these field distributions.

In Sec. II A, we transform the known OBMS parameters into circulant matrices and solve for the unknown field modal vectors. Here, we can perform the inverse procedure by transforming the known field distributions into circulant matrices and solving for the unknown surface property spectra. This leads to the equations

$$\begin{aligned}\frac{1}{2}(\hat{E}_z^t + \hat{E}_z^i + \hat{E}_z^r) = \hat{E}_{\mathrm{av}} &= \mathbf{\Delta}_{\hat{H},\mathrm{in}}\hat{Z}_{\mathrm{SE}} - \mathbf{\Delta}_{\hat{E},\mathrm{in}}\hat{K}_{\mathrm{EM}},\\ \frac{1}{2}(\hat{H}_\phi^t + \hat{H}_\phi^i + \hat{H}_\phi^r) = \hat{H}_{\mathrm{av}} &= \mathbf{\Delta}_{\hat{E},\mathrm{in}}\hat{Y}_{\mathrm{SM}} + \mathbf{\Delta}_{\hat{H},\mathrm{in}}\hat{K}_{\mathrm{EM}},\end{aligned} \tag{17}$$

where $\mathbf{\Delta}_{\hat{E},\mathrm{in}}$ and $\mathbf{\Delta}_{\hat{H},\mathrm{in}}$ are the $N \times N$ field discontinuity circulant matrices formed using the vectors $(\hat{E}_z^t - \hat{E}_z^r - \hat{E}_z^i)$ and $(\hat{H}_\phi^t - \hat{H}_\phi^r - \hat{H}_\phi^i)$, respectively.

An OBMS satisfying LPC will have imaginary $\bar{Z}_{\mathrm{SE}}$ and $\bar{Y}_{\mathrm{SM}}$, as well as real $\bar{K}_{\mathrm{EM}}$ [28]. This allows us to reduce the number of unknowns in Eq. (17) by invoking the conjugate symmetry properties for the DFT of real and imaginary signals:

$$\begin{aligned}\mathrm{Re}\{\bar{V}\} = 0 &\implies \mathbf{F}\hat{V} = -\hat{V}^*,\\ \mathrm{Im}\{\bar{V}\} = 0 &\implies \mathbf{F}\hat{V} = \hat{V}^*,\end{aligned} \tag{18}$$

where $\mathbf{F}$ is the $N \times N$ reversal matrix. Using the fact that $\mathbf{FF} = \mathbf{I}$, we can obtain another system of equation from Eq. (17) as follows:

$$\begin{aligned}\hat{E}_{\mathrm{av}} &= -\mathbf{\Delta}_{\hat{H},\mathrm{in}}\mathbf{F}\hat{Z}_{\mathrm{SE}}^* - \mathbf{\Delta}_{\hat{E},\mathrm{in}}\mathbf{F}\hat{K}_{\mathrm{EM}}^*,\\ \hat{H}_{\mathrm{av}} &= -\mathbf{\Delta}_{\hat{E},\mathrm{in}}\mathbf{F}\hat{Y}_{\mathrm{SM}}^* + \mathbf{\Delta}_{\hat{H},\mathrm{in}}\mathbf{F}\hat{K}_{\mathrm{EM}}^*.\end{aligned} \tag{19}$$

Combining Eq. (17) with the complex conjugate of Eq. (19), we have sufficiently many independent equations to solve for the unknown surface property spectra as

$$\begin{aligned}\hat{K}_{\mathrm{EM}} &= \mathbf{k}_a^{-1}\bar{k}_b,\\ \mathbf{k}_a &= -\left(\mathbf{\Delta}_{\hat{H},\mathrm{in}}^*\mathbf{F}\right)^{-1}(\mathbf{\Delta}_{\hat{E},\mathrm{in}}^*\mathbf{F}) - \mathbf{\Delta}_{\hat{H},\mathrm{in}}^{-1}\mathbf{\Delta}_{\hat{E},\mathrm{in}},\\ \bar{k}_b &= \left(\mathbf{\Delta}_{\hat{H},\mathrm{in}}^*\mathbf{F}\right)^{-1}\hat{E}_{\mathrm{av}}^* + \mathbf{\Delta}_{\hat{H},\mathrm{in}}^{-1}\hat{E}_{\mathrm{av}},\\ \hat{Z}_{\mathrm{SE}} &= \mathbf{\Delta}_{\hat{H},\mathrm{in}}^{-1}\hat{E}_{\mathrm{av}} + \mathbf{\Delta}_{\hat{H},\mathrm{in}}^{-1}\mathbf{\Delta}_{\hat{E},\mathrm{in}}\hat{K}_{\mathrm{EM}},\\ \hat{Y}_{\mathrm{SM}} &= \mathbf{\Delta}_{\hat{E},\mathrm{in}}^{-1}\hat{H}_{\mathrm{av}} - \mathbf{\Delta}_{\hat{E},\mathrm{in}}^{-1}\mathbf{\Delta}_{\hat{H},\mathrm{in}}\hat{K}_{\mathrm{EM}}.\end{aligned} \tag{20}$$

This concludes the synthesis procedure of internally excited passive and lossless OBMS.

C. Multilayer implementations

Having obtained the theoretical OBMS surface parameters in Sec. II B, we now consider a physical unit-cell topology that is suitable for practical realization of the derived properties. For planar metasurfaces, unit cells consisting of three parallel electric impedance sheets separated by dielectric substrates have often been used [29]. It was shown that the unit cell can exhibit omega-bianisotropic response if its three constituent layers are asymmetric with respect to the middle one (i.e., the top and the bottom layers have different impedances). This topology is usually preferred because it is highly compatible with standard PCB fabrication technologies. The three impedance sheets can be easily realized using three layers of etched conductive patterns [8,30]. In this section, we consider an analogous curved triple impedance-layer topology, depicted in Fig. 2.

Each unit cell of the surface is assigned a set of inner, middle, and outer impedance values; they are denoted as $\bar{Z}_i[n]$, $\bar{Z}_m[n]$, and $\bar{Z}_o[n]$, respectively, for the nth cell. The three impedance layers are supported by two cylindrical

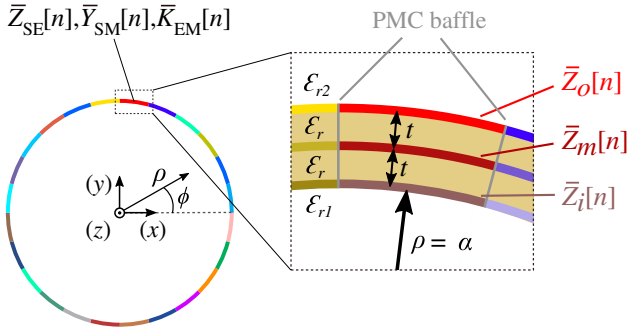

FIG. 2. Triple impedance-layer unit-cell topology used to realize the theoretically derived OBMS properties.

dielectric shells with thickness t and relative permittivity ϵ_r. The inner surface impedances $\bar{Z}_i$ reside on the cylindrical surface $\rho = \alpha$.

For planar OBMSs, equivalent transmission-line models have frequently been used to aid the design of the multilayer unit cells [31]. It is hard to directly adopt this approach here because the wave impedances for cylindrical waves are dependent on the radial coordinate ρ. Thus, they vary throughout the longitudinal extent of each unit cell, making it difficult to construct a simple equivalent transmission-line circuit. Instead, we employ a generalization of the *ABCD* matrix approach previously used to design a mode-converting cylindrical OBMS [32].

Before proceeding, we note that the *ABCD* matrix approach assumes local periodicity. That is, each unit cell is analyzed and designed as if it resides within a homogeneous surface. An accompanying assumption is that only the $p = 0$ mode is propagating between the multiple impedance layers. In a realistic metasurface, due to the ϕ-dependent impedances, local periodicity is not satisfied and higher-order modes can propagate within the extent of each unit cell. This can make the *ABCD* matrix approach inaccurate, especially if the dielectric layers are thick [33]. To alleviate this phenomenon, we employ perfect conducting baffles to shield each unit cell from its neighbors. This approach is inspired by a previous work, which used baffles to decouple the adjacent unit cells in a planar bianisotropic metasurface [34]. As discussed therein, the baffles act as an array of small waveguides, which cut off all but the fundamental mode locally within each unit cell. For the TM^z configuration discussed in this study, perfect magnetic conductor (PMC) baffles are used, as seen in Fig. 2. For TE^z configurations, perfect electric conductor (PEC) baffles are required. While the PEC baffles are more practical since they can be fabricated using plated via fences, PMC baffles mainly serve as numerical tools to aid the validation of theoretically synthesized metasurfaces.

Assuming that the *ABCD* matrix approach is valid, we can apply it to each unit cell individually. The *ABCD* matrix $\mathbf{M}$ between two concentric cylindrical surfaces with radii ρ_1 and ρ_2 relates the *total* electric and magnetic fields on those surfaces according to

$$\begin{bmatrix} E_z(\rho_1) \\ H_\phi(\rho_1) \end{bmatrix} = \mathbf{M} \begin{bmatrix} E_z(\rho_2) \\ H_\phi(\rho_2) \end{bmatrix} = \begin{bmatrix} A & B \\ C & D \end{bmatrix} \begin{bmatrix} E_z(\rho_2) \\ H_\phi(\rho_2) \end{bmatrix}. \quad (21)$$

For instance, the *ABCD* matrix relating the fields on either side of a cylindrical sheet with electric impedance Z is

$$\mathbf{M}_Z = \begin{bmatrix} 1 & 0 \\ -\frac{1}{Z} & 1 \end{bmatrix}. \quad (22)$$

This can be easily derived from the BSTC equations.

We can also find the *ABCD* matrix for the dielectric substrates [26]. If the inner and outer radii of the substrate are ρ_i and ρ_o, respectively, and the relative permittivity is ϵ_r, then the matrix is given by

$$\begin{aligned} \mathbf{M}_{\text{sub}}(\rho_i,\rho_o) &= \begin{bmatrix} A(\rho_i,\rho_o) & B(\rho_i,\rho_o) \\ C(\rho_i,\rho_o) & D(\rho_i,\rho_o) \end{bmatrix} = \mathbf{m}_i \mathbf{m}_o^{-1}, \\ \mathbf{m}_{\{i,o\}}[1][1] &= H_0^{(2)}\left(\sqrt{\epsilon_r} k_o \rho_{\{i,o\}}\right), \\ \mathbf{m}_{\{i,o\}}[1][2] &= J_0\left(\sqrt{\epsilon_r} k_o \rho_{\{i,o\}}\right), \\ \mathbf{m}_{\{i,o\}}[2][1] &= Y_{\text{sub}}^{+}\left(\rho_{\{i,o\}}\right) H_0^{(2)}\left(\sqrt{\epsilon_r} k_o \rho_{\{i,o\}}\right), \\ \mathbf{m}_{\{i,o\}}[2][2] &= Y_{\text{sub}}^{-}\left(\rho_{\{i,o\}}\right) J_0\left(\sqrt{\epsilon_r} k_o \rho_{\{i,o\}}\right), \end{aligned} \quad (23)$$

where

$$\begin{aligned} Y_{\text{sub}}^{+}(\rho) &= -\frac{j\sqrt{\epsilon_r}}{\eta_o} \frac{H_0^{(2)'}(\sqrt{\epsilon_r} k_o \rho)}{H_0^{(2)}(\sqrt{\epsilon_r} k_o \rho)}, \\ Y_{\text{sub}}^{-}(\rho) &= -\frac{j\sqrt{\epsilon_r}}{\eta_o} \frac{J_0'(\sqrt{\epsilon_r} k_o \rho)}{J_0(\sqrt{\epsilon_r} k_o \rho)}. \end{aligned} \quad (24)$$

From Fig. 2, we can see that the matrices $\mathbf{M}_{\text{sub}}(\alpha, \alpha + t)$ and $\mathbf{M}_{\text{sub}}(\alpha + t, \alpha + 2t)$ model the inner and the outer dielectric substrates, respectively. Cascading the matrices for the three impedance layers as well as those for the two dielectric substrates in the appropriate order, we obtain the overall *ABCD* matrix for a unit cell

$$\mathbf{M} = \mathbf{M}_{Z_i} \mathbf{M}_{\text{sub}}(\alpha, \alpha + t) \mathbf{M}_{Z_m} \mathbf{M}_{\text{sub}}(\alpha + t, \alpha + 2t) \mathbf{M}_{Z_o}, \quad (25)$$

where Z_i, Z_m, Z_o are the inner, middle, and outer impedances for that cell, respectively.

Assuming we have already calculated the OBMS parameters $\{Z_{\text{SE}}, Y_{\text{SM}}, K_{\text{EM}}\}$ for the unit cell following the procedures in Sec. II B, we can use Eqs. (8) and (21) to find the

equivalent *ABCD* matrix parameters of that cell as

$$\begin{aligned} A &= \frac{4K_{\mathrm{EM}}^2 + 4Y_{\mathrm{SM}}Z_{\mathrm{SE}} + 4K_{\mathrm{EM}} + 1}{4K_{\mathrm{EM}}^2 + 4Y_{\mathrm{SM}}Z_{\mathrm{SE}} - 1}, \\ B &= \frac{-4Z_{\mathrm{SE}}}{4K_{\mathrm{EM}}^2 + 4Y_{\mathrm{SM}}Z_{\mathrm{SE}} - 1}, \\ C &= \frac{-4Y_{\mathrm{SM}}}{4K_{\mathrm{EM}}^2 + 4Y_{\mathrm{SM}}Z_{\mathrm{SE}} - 1}, \\ D &= \frac{4K_{\mathrm{EM}}^2 + 4Y_{\mathrm{SM}}Z_{\mathrm{SE}} - 4K_{\mathrm{EM}} + 1}{4K_{\mathrm{EM}}^2 + 4Y_{\mathrm{SM}}Z_{\mathrm{SE}} - 1}. \end{aligned} \tag{26}$$

If we denote the elements of dielectric substrate *ABCD* matrices as

$$\begin{aligned} \mathbf{M}_{\mathrm{sub}}(\alpha + t, \alpha + 2t) &= \begin{bmatrix} a_1 & b_1 \\ c_1 & d_1 \end{bmatrix}, \\ \mathbf{M}_{\mathrm{sub}}(\alpha, \alpha + t) &= \begin{bmatrix} a_2 & b_2 \\ c_2 & d_2 \end{bmatrix}, \end{aligned} \tag{27}$$

then the required Z_i, Z_m, and Z_o can be found to be

$$\begin{aligned} Z_i &= \frac{-b_2 B}{b_2 D - d_2 B + a_2 b_1 d_2 - b_1 b_2 c_2}, \\ Z_m &= \frac{b_1 b_2}{a_2 b_1 - B + b_2 d_1}, \\ Z_o &= \frac{b_1 B}{a_1 B - b_1 A - a_1 b_2 d_1 + b_1 b_2 c_1}. \end{aligned} \tag{28}$$

Using Eqs. (26) and (28) on each of the N unit cells gives the final theoretical implementation of our synthesized OBMS.

D. Comments on other metasurface configurations

As mentioned earlier, some of the steps in the analysis and synthesis procedures need to be modified according to the problem geometry. This requirement stems from the fact that the modal expansions of the electric and magnetic fields are problem specific. Furthermore, the BSTC equations, Eq. (8), are different depending on the location of the source (internal or external). This in turn leads to different analysis, Eq. (13), and synthesis, Eq. (20), equations. On the other hand, the *ABCD* matrix formalism presented in Sec. C does not assume anything about the source location, and thus can be used for any problem. As we go over detailed design examples in Sec. III, it becomes clear that the overall DFT framework is readily generalizable.

III. RESULTS AND DISCUSSIONS

In this section, we design several passive and lossless OBMSs using our proposed method and validate them numerically using finite-element simulations in COMSOL Multiphysics. Without loss of generality, we assume henceforth that the external region is comprised of air ($\epsilon_{r2} = 1$).

A. Electromagnetic illusion

In the first example, we design a cylindrical OBMS, which transforms the fields radiated by an electric line source located at the origin to those from a displaced line source. Previously, metamaterials (MTMs) based on transformation optics (TO) have been leveraged to achieve this effect [35]. However, the practicality of TO MTMs is significantly hindered by their bulkiness and complexity. Here, we attempt to achieve the same electromagnetic illusion using a metasurface with deeply subwavelength thickness, which is much easier to fabricate and deploy. Although this type of device has been widely reported [20,23,24], passive lossless implementations leveraging omega-bianisotropy have not been demonstrated thus far.

To design the illusion metasurface, we first state the incident electric field modal vector as

$$\hat{E}_z^i[n] = e_0^i \delta_{n^\star,0}, \tag{29}$$

where $n^\star$ is as defined in Eq. (6) and $\delta_{i,j}$ is the Kronecker delta. The complex amplitude e_0^i can be arbitrarily chosen. There is only one nonzero entry in $\hat{E}_z^i$ because an electric line source located at the origin can only excite the 0th cylindrical mode.

The transmitted modal vector can be obtained using the addition theorem, which describes a Hankel function centered at $(\rho, \phi) = (\rho', \phi')$ in terms of a summation of cylindrical modes centered at the origin [36]:

$$H_0^{(2)}(k_o|\vec{\rho} - \vec{\rho}'|) = \begin{cases} \displaystyle\sum_{p=-\infty}^{\infty} J_p(k_o\rho')H_p^{(2)}(k_o\rho)e^{jp(\phi-\phi')} & \rho \geq \rho' \quad \text{(30a)} \\ \displaystyle\sum_{p=-\infty}^{\infty} H_p^{(2)}(k_o\rho')J_p(k_o\rho)e^{jp(\phi-\phi')} & \rho \leq \rho'. \quad \text{(30b)} \end{cases}$$

For the case of a virtual source located inside the OBMS cavity ($\rho' < \alpha$), we can obtain $\hat{E}_z^t$ using Eq. (30a) by setting $\rho = \alpha$:

$$\hat{E}_z^t[n] = e_0^t \frac{J_{n^\star}(k_o\rho')H_{n^\star}^{(2)}(k_o\alpha)}{H_0^{(2)}(k_o\alpha)} e^{jn^\star\phi'}. \tag{31}$$

The coefficient e_0^t is the amplitude of the virtual source field measured at a distance α away from $\vec{\rho}\,'$; it is set to be equal to e_0^i in this study. As an example, we design an illusion metasurface with the specifications listed in Table I. Since this is a transmissive metasurface, we solve for the required auxiliary $\hat{E}_z^r$ using Eq. (15). The numerically obtained solution is shown in Fig. 3(a). Using the complete

TABLE I. Specification for the passive lossless illusion OBMS.

f (GHz)	N	α (m)	ρ'	ϕ' (rad)	ϵ_{r1}	ϵ_{r2}	ϵ_r	t (mm)
4.4	451	0.15	0.95α	$\pi/4$	2.2	1	3	0.2

field distributions $\hat{E}_z^{\{i,t,r\}}$, we obtain the multilayer implementation for the OBMS described by Fig. 3(b). Notably, we only plot the reactances of each layer, since the real parts of the impedances are identically zero. This indicates the synthesized device is truly passive and lossless.

Next, we construct the metasurface model in COMSOL Multiphysics, in which the surface reactance layers are implemented using field-dependent surface electric current densities. The source is an electric line current placed at the origin. The simulated total (incident plus scattered) electric field distribution is depicted in Fig. 4. Despite the complex interference pattern produced by the auxiliary internal reflections, we observe clear unperturbed wavefronts outside of the metasurface cavity emanating from the desired virtual source location.

In some scenarios, one may wish to construct a virtual source outside of the OBMS cavity ($\rho' > \alpha$). Although at first it appears that Eq. (30b) should be used to obtain $\hat{E}_z^t$, we note that such a field distribution cannot actually be realized with an internally excited OBMS. This is because Eq. (30b), and indeed the fields of an ideal external virtual line source, exhibit converging power flow (towards the origin) for some points on the external face of the metasurface. This can be seen from the Bessel functions, which constitute the summation in Eq. (30b), or it can be reasoned intuitively by the fact that the Poynting vector should strictly diverge from (ρ', ϕ'). We can circumvent this issue by approximating the desired external field distribution using Eq. (30a). Following the same synthesis procedure, we can obtain an OBMS whose external fields imitate those of the desired virtual source for the region $\rho \geq \rho'$. However, in the region $\alpha < \rho < \rho'$, the fields will not accurately depict the desired virtual source fields.

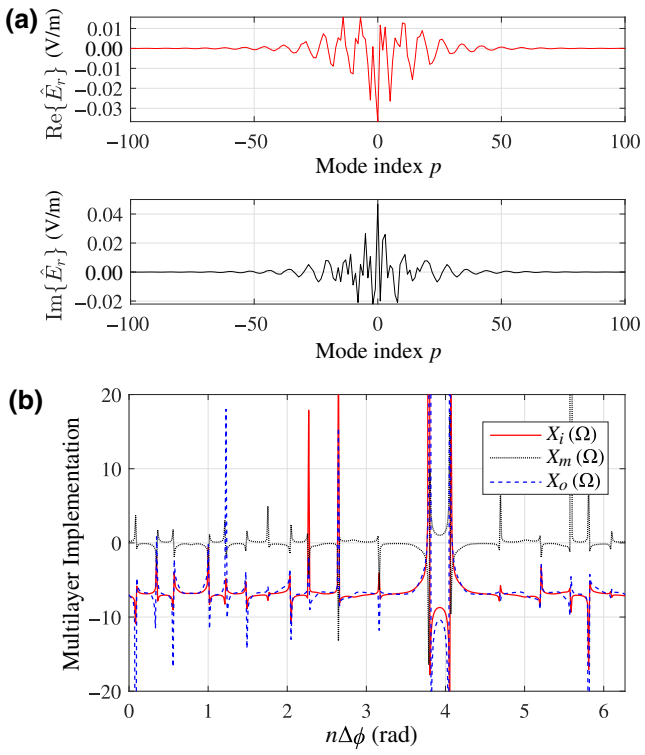

FIG. 3. (a) The solved auxiliary reflected fields for the illusion OBMS. Higher-order modes with near-zero amplitudes are omitted. (b) The reactance values for the multilayer implementation of the illusion OBMS.

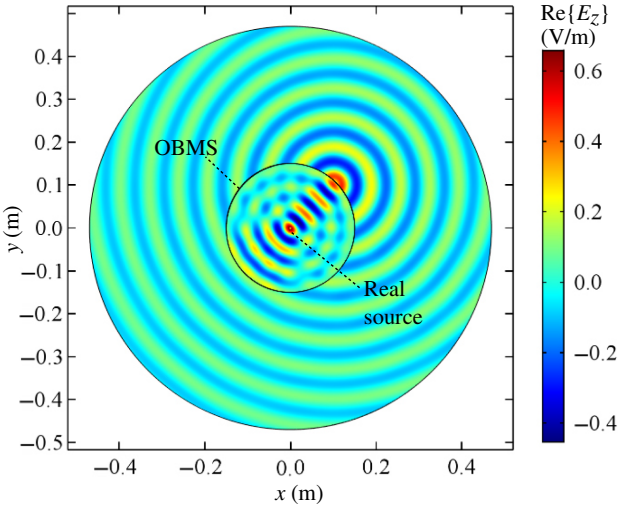

FIG. 4. Re{E_z} for the illusion OBMS.

B. General penetrable metasurface cloak

In this example, we design a metasurface cloak, which conceals a cylindrical target from an external incident wave. Conventionally, this is often achieved with active Huygens' metasurfaces (HMS), which radiate some prescribed fields intended to destructively interfere with the scattered fields from the target [14,37]. While effective, this type of cloak usually requires complex circuitry to properly control and can suffer from stability issues. Alternatively, TO MTM cloaks have also been demonstrated [38]. They are highly robust, capable of concealing the target from any illumination type with any incident direction. However, just like other MTM-based devices, their bulkiness significantly restricts their practical applications.

Recently, a type of penetrable metasurface cloak has been demonstrated [15]. It was proposed that if the object is penetrable by electromagnetic waves, one can synthesize a metasurface enclosure, which induces zero external scattered fields while permitting some internal scattering. By carefully engineering the internal fields based on the

incident fields, which are known *a priori*, local power conservation can be satisfied. Thus, the cloak can be realized using a passive and lossless OBMS. A useful application for this class of cloaking is the reduction of electromagnetic interference for complex wireless communications systems in which the incident field distributions are known [39].

Previous literature on penetrable OBMS cloaks assume the incident field to be a perfect plane wave. In that case, the required internal fields for satisfying local power conservation can be easily inferred to be another plane wave. Here, we extend this concept in two ways. First, we allow the incident fields to take on arbitrary forms. In general, the required internal fields for satisfying local power conservation are intricate and lack analytical descriptions. With our proposed approach, we can specify the reflected fields to be zero and numerically solve the local power conservation equation to obtain the required internal (auxiliary) fields. This straightforward procedure enables us to hide the object from more complex illuminations.

Furthermore, with some slight modifications, we can realize perfect cloaking for an impenetrable object such as a PEC cylinder. Although passive and lossless metasurfaces with such capability have been demonstrated [16], they rely on carefully optimized orthogonally polarized surface waves facilitated by tensorial surface properties to achieve point-wise power balance. In contrast, our proposed approach uses a scalar metasurface, which does not rely on any polarization conversion. In that light, our approach is similar to a previous work that leverages auxiliary transmitted waves to facilitate satisfaction of local power conservation in a reflective metasurface beam splitter [6]. Scalar metasurfaces can be easier to fabricate in practice compared to tensorial surfaces, owing to the simpler geometries of their constituent meta-atoms.

To develop the penetrable cloak, let us first consider the case of a general externally excited cylindrical OBMS enclosing a homogeneous dielectric cylinder, as depicted in Fig. 5. Unlike the problem in Sec. A, the incident and reflected fields now exist in the external region whereas the transmitted fields exist in the internal region, meaning the definitions in Eq. (4) need to be adjusted accordingly. Furthermore, the BSTC equations for this problem read

$$\begin{aligned}\frac{1}{2}(\bar{E}_z^i+\bar{E}_z^r+\bar{E}_z^t)&=\bar{Z}_{\rm SE}\odot(\bar{H}_\phi^i+\bar{H}_\phi^r-\bar{H}_\phi^t)\\&\quad-\bar{K}_{\rm EM}\odot(\bar{E}_z^i+\bar{E}_z^r-\bar{E}_z^t),\\\frac{1}{2}(\bar{H}_\phi^i+\bar{H}_\phi^r+\bar{H}_\phi^t)&=\bar{Y}_{\rm SM}\odot(\bar{E}_z^i+\bar{E}_z^r-\bar{E}_z^t)\\&\quad+\bar{K}_{\rm EM}\odot(\bar{H}_\phi^i+\bar{H}_\phi^r-\bar{H}_\phi^t).\end{aligned}\tag{32}$$

The new source location implies that the incident and the transmitted fields are now composed of $J_p(\cdot)$, while the reflected fields are described by $H_p^{(2)}(\cdot)$. The wave number for those fields also need to be changed accordingly to reflect the appropriate dielectric constants in the internal and external regions. Combining these observations, the modal admittance matrices can be inferred to be

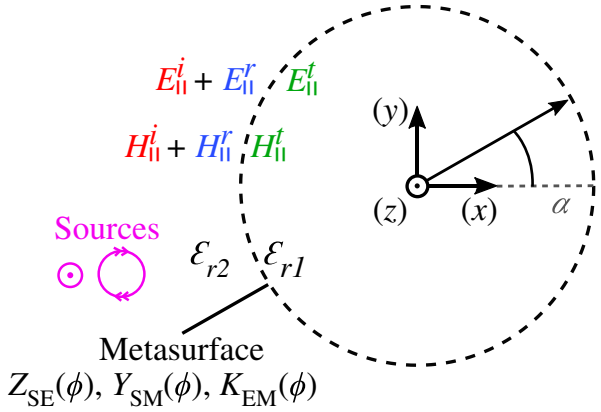

FIG. 5. Geometric configuration of the externally excited cylindrical OBMS.

$$\begin{aligned}\mathbf{Y}_{\rm ex}^{\{i,t,r\}}&=\mathrm{diag}\left[Y_{{\rm ex},p_-}^{\{i,t,r\}}(\alpha)\quad\cdots\quad Y_{{\rm ex},p_+}^{\{i,t,r\}}(\alpha)\right]^T,\\Y_{{\rm ex},p}^i(\rho)&=-\frac{j\sqrt{\epsilon_{r2}}}{\eta_o}\frac{J_p'(k_2\rho)}{J_p(k_2\rho)},\\Y_{{\rm ex},p}^r(\rho)&=-\frac{j\sqrt{\epsilon_{r2}}}{\eta_o}\frac{H_p^{(2)'}(k_2\rho)}{H_p^{(2)}(k_2\rho)},\\Y_{{\rm ex},p}^t(\rho)&=-\frac{j\sqrt{\epsilon_{r1}}}{\eta_o}\frac{J_p'(k_1\rho)}{J_p(k_1\rho)}.\end{aligned}\tag{33}$$

The subscript "ex" indicates that these matrices are valid for externally excited OBMSs.

Following the same convolution-based derivation presented in Sec. II A, we can obtain modal transmission matrix $\hat{\mathbf{T}}_{\rm ex}$ and modal reflection matrix $\hat{\mathbf{R}}_{\rm ex}$ for this new configuration. Although these matrices are not explicitly used in this paper, we still present their full solutions in Appendix A for completeness; they are given by Eqs. (A1) and (A2), respectively.

To synthesize an externally excited cylindrical OBMS, we again need to solve the appropriate local power conservation equation, Eq. (15) or Eq. (16), for the required auxiliary fields. However, now we need to pay attention to substitute $\mathbf{Y}_{\rm ex}^t$ in place of $\mathbf{Y}_{\rm in}^t$, and $\mathbf{Y}_{\rm ex}^r$ in place of $\mathbf{Y}_{\rm in}^r$. After the fields everywhere are known, we use Eq. (20) to evaluate $\{\bar{Z}_{\rm SE},\bar{Y}_{\rm SM},\bar{K}_{\rm EM}\}$. Due to the transposed locations of the incident, transmitted, and reflected fields, new field discontinuity circulant matrices $\mathbf{\Delta}_{\hat{E},{\rm ex}}$ and $\mathbf{\Delta}_{\hat{H},{\rm ex}}$ need to be used in place of $\mathbf{\Delta}_{\hat{E},{\rm in}}$ and $\mathbf{\Delta}_{\hat{H},{\rm in}}$, where

$$\mathbf{\Delta}_{\hat{E},{\rm ex}}=-\mathbf{\Delta}_{\hat{E},{\rm in}},\quad\mathbf{\Delta}_{\hat{H},{\rm ex}}=-\mathbf{\Delta}_{\hat{H},{\rm in}}.\tag{34}$$

TABLE II. Specification for the passive lossless penetrable OBMS cloak for concealing a dielectric cylinder.

f (GHz)	N	α (m)	ρ_s(m)	ϕ_s (rad)	ϵ_{r1}	ϵ_{r2}	ϵ_r	t (mm)
4.4	451	0.15	0.2	0	3	1	3	0.2

Last but not least, the conversion from OBMS parameters $\{\bar{Z}_{\rm SE}, \bar{Y}_{\rm SM}, \bar{K}_{\rm EM}\}$ to three-layer impedance implementation $\{\bar{Z}_i, \bar{Z}_m, \bar{Z}_o\}$ can be done with Eqs. (26) and (28) without any modifications.

Now, let us apply this general procedure to design a penetrable OBMS cloak, which conceals a dielectric cylinder with permittivity ϵ_{r1} from an external line source located at $(\rho, \phi) = (\rho_s, \phi_s)$. We first write the incident field modal vector with Eq. (30b):

$$\hat{E}_z^i[n] = e_0^i H_{n^\star}^{(2)}(k_o\rho_s) J_{n^\star}(k_o\alpha) e^{jn^\star\phi_s}, \tag{35}$$

where $n^\star$ is as defined in Eq. (6). The coefficient e_0^i can be set to some arbitrary constant. Since the goal is to produce zero external scattered field, the desired reflected modal vector must be $\hat{E}_z^r = 0$. As this is a reflective metasurface, we need to solve Eq. (16) for the required $\hat{E}_z^t$. Assuming the configuration as described in Table II, we obtain the auxiliary transmitted field modal vector to be that depicted in Fig. 6(a). Using these values, we obtain the three impedance layers depicted in Fig. 6(b). Again, the real parts are omitted since they are identically zero.

To validate this design, we first simulate the scattering from the dielectric cylinder without the OBMS cloak. The total electric field distribution is shown in Fig. 7(a). As seen by the highly perturbed wavefronts, the cylinder interferes with the source radiation to a significant degree. Next, we add the OBMS around the dielectric cylinder and resimulate with the same source. The resulting fields are shown in Fig. 7(b). Evidently, there is almost no scattering from the cylinder observable in the external region. The object appears essentially invisible to any observer outside of the cylindrical volume.

Next, we continue the development of more advanced penetrable metasurface cloaks by designing a passive and

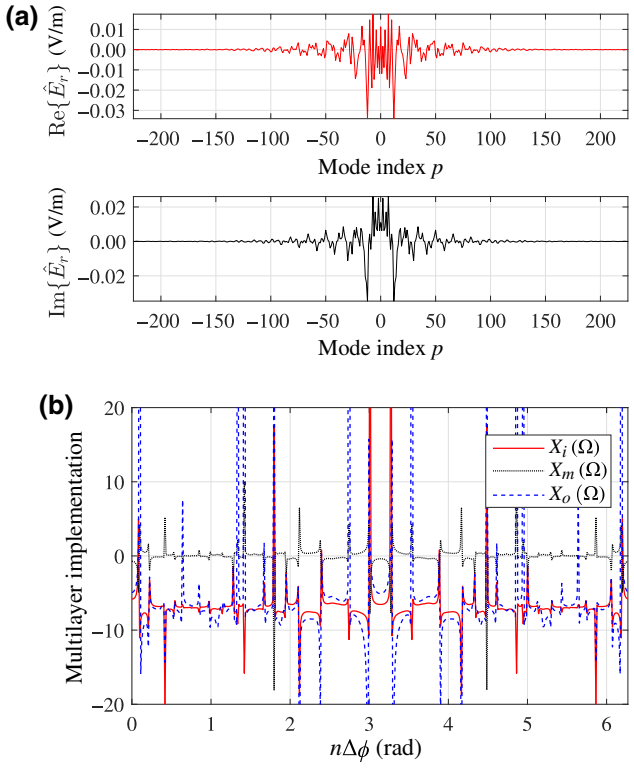

FIG. 6. (a) The solved auxiliary transmitted fields for the penetrable OBMS cloak. (b) The reactance values for the multilayer implementation of the cloak.

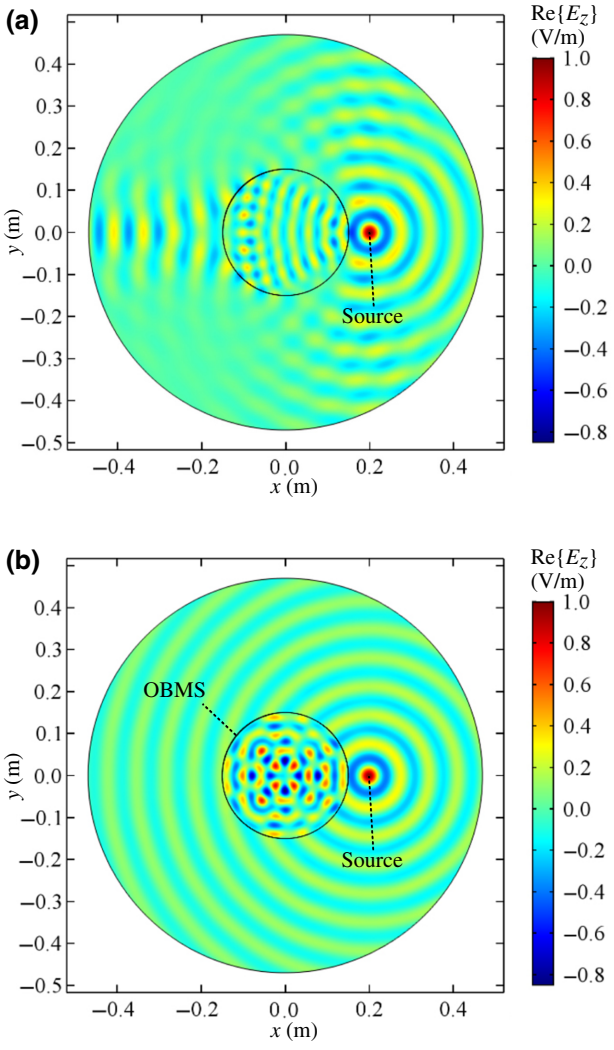

FIG. 7. Re{E_z} for the dielectric cylinder (a) without the OBMS cloak; and (b) with the OBMS cloak.

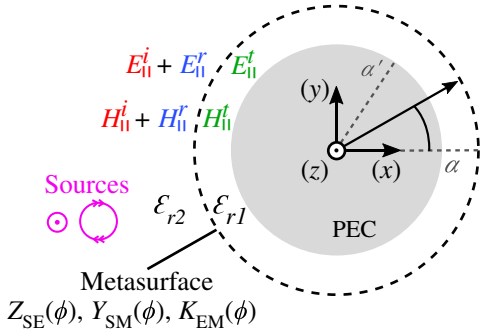

FIG. 8. Schematic for the penetrable OBMS cloak for a PEC cylinder.

lossless OBMS, which perfectly conceals a PEC cylinder from a known source. This can be challenging since the target itself does not permit any internal fields, meaning it is generally impossible to satisfy Eq. (16). However, if we insert a small gap between the PEC cylinder and the OBMS, as depicted in Fig. 8, then both sides of the cloak can support nonzero fields. Practically, this small gap can represent an air gap or a dielectric coating around the target. There is no inherent restriction on its thickness.

We first identify the modal admittance matrices for this problem. Since the incident and reflected fields of all externally excited OBMSs have the same constituent wave functions, we have

$$\mathbf{Y}^i_{\mathrm{PEC}} = \mathbf{Y}^i_{\mathrm{ex}}, \quad \mathbf{Y}^r_{\mathrm{PEC}} = \mathbf{Y}^r_{\mathrm{ex}}, \tag{36}$$

where the subscript "PEC" indicates that these expressions are valid for OBMSs surrounding a PEC cylinder.

Due to the inclusion of the PEC, the transmitted fields are now described by a linear combination of Bessel (J_p) and Neumann (Y_p) functions, which satisfy $E_z(\alpha', \phi) = 0$, where α' is the radius of the PEC cylinder. The explicit modal expansions for the fields can be written as

$$\begin{aligned} E^t_z(\rho,\phi) &= \sum_{p=-\infty}^{\infty} e^t_p \left[\frac{Y_p(k_1\alpha')}{d_p(k_1\alpha', k_1\alpha)} J_p(k_1\rho) \right. \\ &\quad \left. - \frac{J_p(k_1\alpha')}{d_p(k_1\alpha', k_1\alpha)} Y_p(k_1\rho) \right] e^{-jp\phi}, \\ H^t_z(\rho,\phi) &= \sum_{p=-\infty}^{\infty} e^t_p \frac{j\sqrt{\epsilon_{r1}}}{\eta_o} \left[\frac{Y_p(k_1\alpha')}{d_p(k_1\alpha', k_1\alpha)} J'_p(k_1\rho) \right. \\ &\quad \left. - \frac{J_p(k_1\alpha')}{d_p(k_1\alpha', k_1\alpha)} Y'_p(k_1\rho) \right] e^{-jp\phi}, \\ d_p(r_1, r_2) &= Y_p(r_1)J_p(r_2) - Y_p(r_2)J_p(r_1). \end{aligned} \tag{37}$$

Recalling that the modal vectors represent the NDFT of the sampled fields at $\rho = \alpha$, we can write

$$\begin{aligned} \hat{E}^t_z &= \begin{bmatrix} e^t_{p_-} & \cdots & e^t_{p_+} \end{bmatrix}^T = \mathbf{\Gamma}_a \hat{E}^t_z - \mathbf{\Gamma}_b \hat{E}^t_z, \\ \mathbf{\Gamma}_a &= \mathrm{diag}\left[\frac{Y_{p_-}(k_1\alpha')J_{p_-}(k_1\alpha)}{d_{p_-}(k_1\alpha', k_1\alpha)} \quad \cdots \quad \frac{Y_{p_-}(k_1\alpha')J_{p_-}(k_1\alpha)}{d_{p_-}(k_1\alpha', k_1\alpha)} \right]^T, \\ \mathbf{\Gamma}_b &= \mathrm{diag}\left[\frac{Y_{p_-}(k_1\alpha)J_{p_-}(k_1\alpha')}{d_{p_-}(k_1\alpha', k_1\alpha)} \quad \cdots \quad \frac{Y_{p_-}(k_1\alpha)J_{p_-}(k_1\alpha')}{d_{p_-}(k_1\alpha', k_1\alpha)} \right]^T, \end{aligned} \tag{38}$$

and

$$\begin{aligned} \hat{H}^t_z &= \mathbf{y}^t_{\mathrm{PEC},a} \mathbf{\Gamma}_a \hat{E}^t_z - \mathbf{y}^t_{\mathrm{PEC},b} \mathbf{\Gamma}_b \hat{E}^t_z \triangleq \mathbf{Y}^t_{\mathrm{PEC}} \hat{E}^t_z, \\ \mathbf{y}^t_{\mathrm{PEC},a} &= -\frac{j\sqrt{\epsilon_{r1}}}{\eta_o} \times \mathrm{diag}\left[\frac{J'_{p_-}(k_1\alpha)}{J_{p_-}(k_1\alpha)} \quad \cdots \quad \frac{J'_{p_+}(k_1\alpha)}{J_{p_+}(k_1\alpha)} \right]^T, \\ \mathbf{y}^t_{\mathrm{PEC},b} &= -\frac{j\sqrt{\epsilon_{r1}}}{\eta_o} \times \mathrm{diag}\left[\frac{Y'_{p_-}(k_1\alpha)}{Y_{p_-}(k_1\alpha)} \quad \cdots \quad \frac{Y'_{p_+}(k_1\alpha)}{Y_{p_+}(k_1\alpha)} \right]^T, \end{aligned} \tag{39}$$

where $\mathbf{Y}^t_{\mathrm{PEC}}$ is the new transmitted modal admittance matrix for this particular problem.

Noting that the BSTCs given by Eq. (32) still apply, we can reuse the expressions (A1) and (A2) to construct the modal transmission matrix $\hat{\mathbf{T}}_{\mathrm{PEC}}$ and modal reflection matrix $\hat{\mathbf{R}}_{\mathrm{PEC}}$ of the present configuration, simply by substituting $\mathbf{Y}^{\{t,t,r\}}_{\mathrm{PEC}}$ in place of $\mathbf{Y}^{\{i,t,r\}}_{\mathrm{ex}}$.

As the first step of the synthesis procedure, we find the required auxiliary $\hat{E}^t_z$ with Eq. (16), by replacing $\mathbf{Y}^t_{\mathrm{in}}$ with $\mathbf{Y}^t_{\mathrm{PEC}}$. Since it is still an externally excited OBMS, we can use Eq. (20) by replacing $\mathbf{\Delta}_{\hat{E},\mathrm{in}}$ and $\mathbf{\Delta}_{\hat{H},\mathrm{in}}$ with $\mathbf{\Delta}_{\hat{E},\mathrm{ex}}$ and $\mathbf{\Delta}_{\hat{E},\mathrm{ex}}$, as is done previously for the dielectric cylinder cloak. This gives the required OBMS parameters $\{\bar{Z}_{\mathrm{SE}}, \bar{Y}_{\mathrm{SM}}, \bar{K}_{\mathrm{EM}}\}$. In the last step, we convert these parameters to the three-layer impedance implementation $\{\bar{Z}_i, \bar{Z}_m, \bar{Z}_o\}$ using Eqs. (26) and (28) without any modifications.

Following the aforementioned procedure, we design an OBMS cloak with the specifications outlined in Table III. The solved modal vector for the required auxiliary $\hat{E}^t_z$ is shown in Fig. 9(a). The corresponding passive and lossless multilayer implementation is shown in Fig. 9(b). Inserting these reactance values into a COMSOL model and simulating with the designated incident fields, we obtain the electric field distribution shown in Fig. 10(a). Note that for better legibility, the fields inside the dielectric coating

TABLE III. Specification for the passive lossless OBMS cloak for concealing a PEC cylinder.

f (GHz)	N	α (m)	α' (m)	ρ_s (m)	ϕ_s	ϵ_{r1}	ϵ_{r2}	ϵ_r	t (mm)
4.4	401	0.1025	0.1	0.2	0	2.2	1	3	0.2

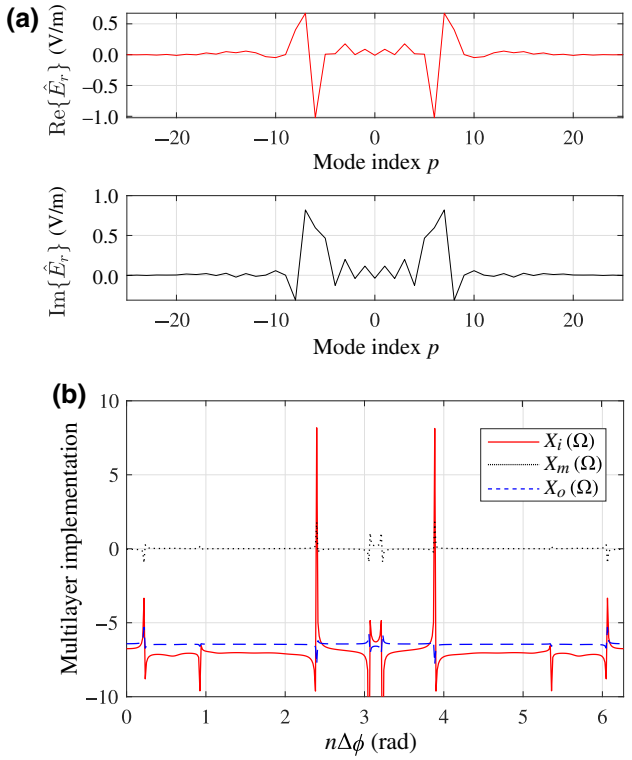

FIG. 9. (a) The solved auxiliary transmitted field for the penetrable OBMS cloak around a PEC cylinder. Higher-order modes with near-zero amplitudes are omitted. (b) The reactance values for the multilayer implementation of the cloak.

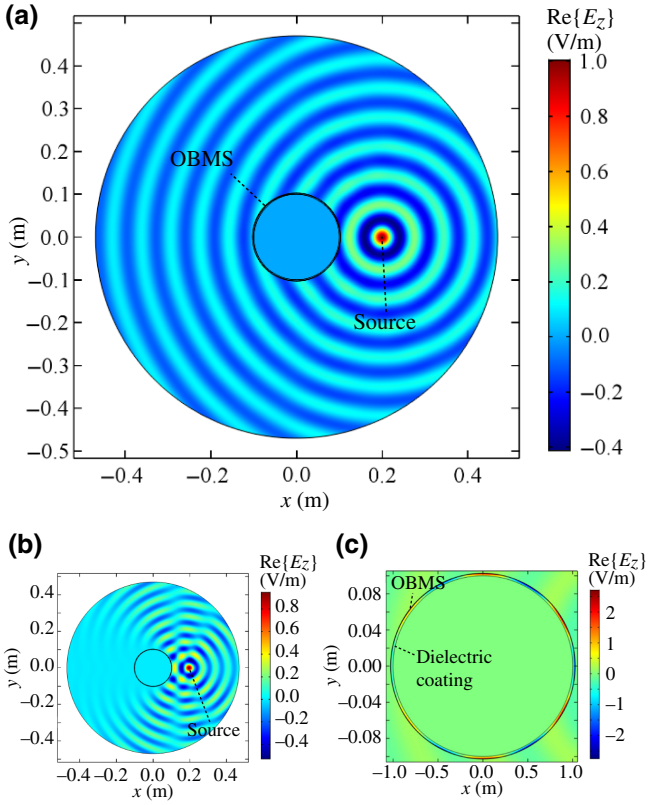

FIG. 10. (a) Re{E_z} for the PEC cylinder with the OBMS cloak. The fields inside the dielectric coating region is omitted here and plotted in (c) instead. (b) Re{E_z} for the PEC cylinder without the OBMS cloak.

region have been excluded from this plot. The unperturbed external wavefronts signify the successful concealment of the PEC cylinder. For comparison, the fields without the OBMS cloak is shown in Fig. 9(b), in which the PEC cylinder casts a significant shadow. As illustrated in Fig. 10(c), the dielectric coating region around the PEC contains high-intensity waves corresponding to the auxiliary fields. The amplitudes of the internal waves can be reduced by increasing the coating thickness. Nevertheless, this evidently does not impair the intended functionality of the OBMS cloak.

C. High-gain cavity-excited antenna

In the last example, we design a cylindrical OBMS cavity, which significantly enhances the directivity of an electric line source that would otherwise produce omnidirectional radiations by itself. Previously, low-profile designs with rectangular cavities have been presented [17,40]. Here, we extend this idea to a cylindrical topology, which can be useful in direction-finding and navigation systems or radio beacons.

To demonstrate the use of OBMS in constructing high-gain antennas, let us design a surface that collimates the cylindrical radiation into a directive beam towards some angle ϕ_o. Since the incident fields are again those produced by a line source placed at the origin, the modal vector is described by Eq. (29). The desired transmitted fields can be obtained by first identifying an envelope for its magnitude around the circumference of the cavity. For simplicity, let us assume it to be an azimuthal box function centered at $\phi = 0$, with extent Φ:

$$|E_z^t(\rho = \alpha^+, \phi)| = \begin{cases} e_o & 0 < \phi \le \frac{\Phi}{2}, \quad (40a) \\ 0 & \frac{\Phi}{2} < \phi \le 2\pi - \frac{\Phi}{2}, \quad (40b) \\ e_o & 2\pi - \frac{\Phi}{2} < \phi \le 2\pi. \quad (40c) \end{cases}$$

Note that a more sophisticated envelope function than Eq. (40) might lead to higher maximum directivity. This is reserved for future studies.

Next, we need to properly phase the output field in order to produce the desired directional radiation. This can be done by sampling the phase of a plane wave traveling towards ϕ_o:

$$\angle E_z^t(\rho = \alpha^+, \phi) = -k_o \alpha \cos\left[\phi - \phi_o\right]. \quad (41)$$

Equations (40) and (41) can be used in conjunction to obtain the desired transmitted modal vector $\hat{E}_z^t$. Since this

TABLE IV. Specification for the cavity-excited OBMS antenna.

f (GHz)	N	α (m)	ϕ_o	Φ (rad)	ϵ_{r1}	ϵ_{r2}	ϵ_r	t (mm)
4.4	451	0.15	0	π	1	1	3	0.2

is classified as an internally excited transmissive metasurface, we solve Eq. (15) to find the required auxiliary reflections. Assuming the specifications are as shown in Table IV, we calculate the reflected fields to be those depicted in Fig. 11(a). Correspondingly, the reactance values of the three-layer implementation of the OBMS antenna are shown in Fig. 11(b). Interestingly, for the angular range $\pi/2 < \phi < 3\pi/2$, the inner layer has near-zero reactance, meaning that essentially half of the OBMS cavity behaves as a PEC backing. It is consistent with intuition, since the amplitude envelope for the transmitted fields in that region is set to zero. The outer- and middle-layer reactance values for that region in fact have very little influence on the radiation pattern of the antenna.

Next, we numerically validate this design in COMSOL. In Fig. 12, we show the simulated total electric field distribution of the antenna when it is fed by an electric line source located at the origin. The omnidirectional source

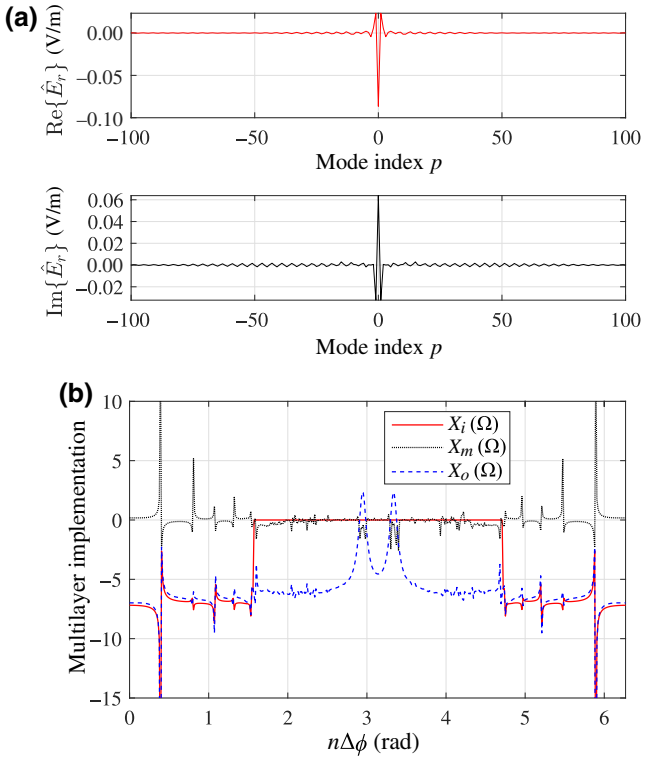

FIG. 11. (a) The solved auxiliary reflected fields for the cavity-excited OBMS antenna. Higher-order modes with near-zero amplitudes are omitted. (b) The reactance values for the multilayer implementation of the OBMS antenna.

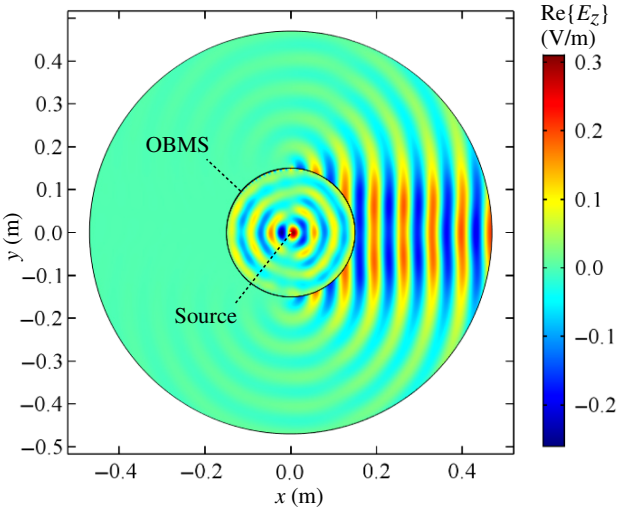

FIG. 12. Re{E_z} for the cavity-excited OBMS antenna.

field is collimated into a highly directive beam pointed at ϕ_o.

The directivity plot of the complete antenna system is shown in Fig. 13. The maximum 2D directivity is 13.4 dBi, a significant improvement over that of the omnidirectional line source. The half power beam width is approximately 7.5°.

D. Additional comments

Although we consider only TM^z-polarized fields in this paper, it is easy to see that the proposed framework can be readily extended to TE^z configurations. One simply needs to modify the modal admittance matrices in accordance with the cylindrical wave functions of the TE^z fields. Furthermore, it is possible to model and design tensorial

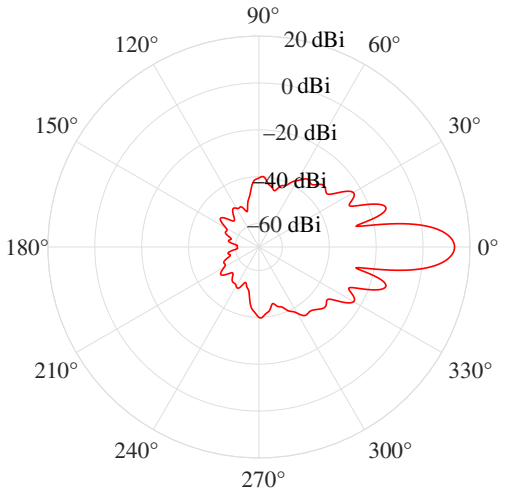

FIG. 13. 2D directivity plot of the cavity-excited OBMS antenna.

TABLE V. Design parameters for the practical PCB-based illusion OBMS.

f (GHz)	N	α	ρ'	ϕ'	ϵ_{r1}	ϵ_{r2}	ϵ_r	t (mm)
10	21	$\lambda_o/2$	0.95α	0	1	1	3	0.127

bianisotropic metasurfaces, which simply involve more equations and more unknowns.

IV. PRACTICAL REALIZATION

To demonstrate the viability of the presented OBMS designs, we discuss a possible practical implementation of the electromagnetic illusion surfaces introduced in Sec. A. As remarked previously, the passive and lossless nature of our designs enables us to fabricate their constituent unit cells using three stacked layers of metallic patterns etched on two bonded sheets of PCBs. To engineer these patterns, we first assume the design specifications listed in Table V, and evaluate the required reactance profiles on each layer. The resulting reactances for the $N = 21$ unit cells are plotted in Fig. 14. The symmetry about cell number 1 implies that only 11 unique cell designs are needed.

We observe in Fig. 14 that the inner and the outer layers contain only negative reactance values, which suggests that they can be realized using capacitive gaps perpendicular to the electric field direction (z axis). The middle layer can have positive or negative reactance values and thus demand more careful treatment. For unit cells with inductive X_m values, we place a meandering inductor on the middle layer, as depicted in Fig. 15. This type of unit-cell design is referred to as "type A." For cells requiring more capacitive values of X_m, a loaded dipole such as that shown in Fig. 16 is used. These cells are referred to as "type B." The dipoles are used for type-B cells instead

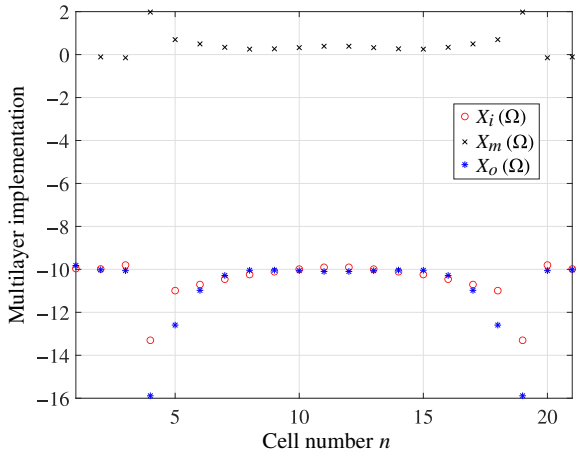

FIG. 14. The reactance values for the practical multilayer implementation of the illusion OBMS.

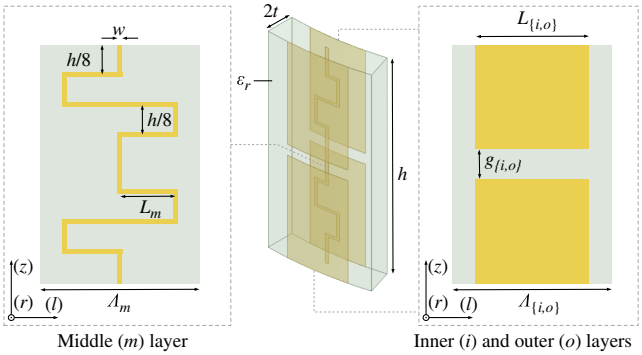

FIG. 15. Schematic for a type-A unit cell.

of simple capacitive gaps because they bear closer resemblance to the inductors of type-A cells. This may lead to better performance for the overall device due to less severe violation of the local periodic assumption. Additionally, the dipole resonances also allow type-B cells to realize near-zero positive values of X_m, which are difficult to realize using type-A cells. In both of Figs. 15 and 16, the coordinate l indicates the horizontal arc length across the cylindrical surface.

To design each of the unit cells, it is necessary to establish a mapping between their geometric features and their effective reactance values. To do this, we use the simulation setup shown in Fig. 17, which was previously leveraged to design acoustic metasurfaces [32]. In accordance with the local periodic assumption, we place a single unit cell in a wedge of a radial waveguide, and illuminate it with the 0th-mode TM^z cylindrical wave. If the unit-cell area is electrically small, the scattered fields, observed away from the OBMS, will contain only the 0th TM^z mode. Thus, by evaluating the total electric fields at each of the three probe planes indicated in Fig. 17, we can obtain the coefficients e_0^i, e_0^t, and e_0^r. They can be used to specify the boundary electromagnetic fields in the BSTCs equations, leading to solutions for the effective $\{Z_{\mathrm{SE}}, Y_{\mathrm{SM}}, K_{\mathrm{EM}}\}$ of the unit cell under test. Lastly, we can use Eq. (28) to extract its effective $\{X_i, X_m, X_o\}$.

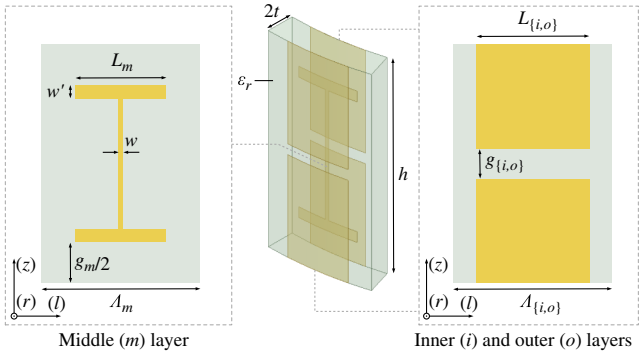

FIG. 16. Schematic for a type-B unit cell.

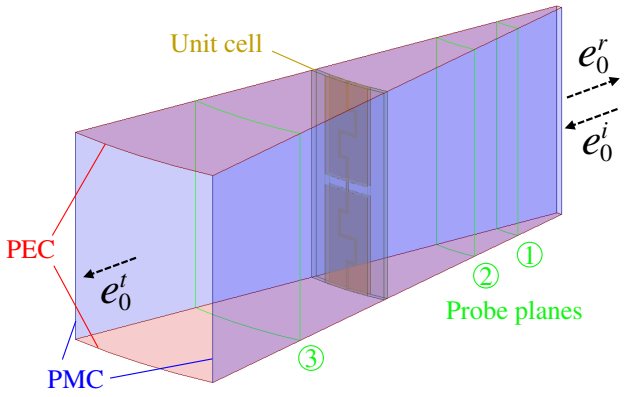

FIG. 17. Simulation setup used to characterize the effective $\{X_i, X_m, X_o\}$ of a three-layer OBMS unit cell.

Having established a method to obtain the effective parameters of a unit-cell design, we can iteratively tune its geometric features until the desired characteristics as specified in Fig. 14 are observed. Repeating this process for the 11 unique cell designs, we arrive at the overall OBMS illustrated in Fig. 18. Here, a single slice of the z-periodic device is shown. The subwavelength height of the unit cells ($h = 10$ mm) means that the complete design, consisting of stacked periodic repetition of the depicted slice, can be considered as homogeneous along the z direction. A complete summary of the geometric parameters of this design is given in Appendix B.

In order to account for the impact of conductor losses, which have been neglected thus far, we realize the conductive portions of the meta-atoms using metallic patterns with finite conductivity 5.8×10^7 S/m (copper). We also introduce dielectric losses by setting the loss tangent of the substrate to 0.0013, which corresponds to that of the Rogers RO3003 laminate.

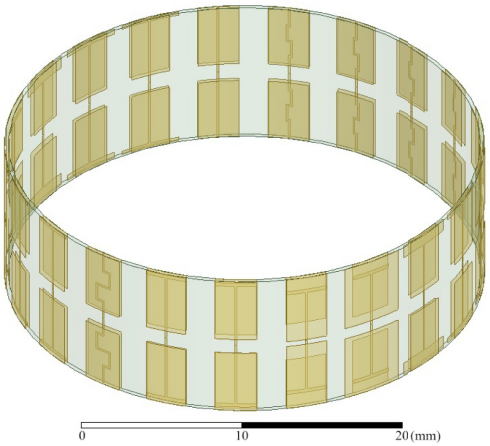

FIG. 18. A horizontal slice of the practical electromagnetic illusion OBMS. The complete design consists periodic repetition of the ring along the axial direction.

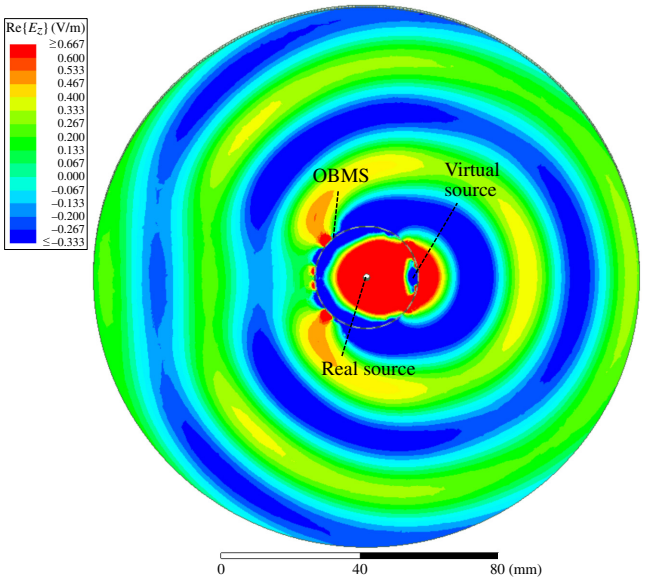

FIG. 19. Re{E_z} for the practical illusion OBMS design of Fig. 18.

To characterize the performance of this design, we place the slice depicted in Fig. 18 into an infinitely large radial waveguide with height h and excite a z-polarized cylindrical wave emanating from the origin. An x-y plane cut of the resultant total electric field distribution, obtained from full-wave simulations using Ansys HFSS, is plotted in Fig. 19. The external fields indeed appear as if they are radiated by a virtual source located at $\vec{\rho}\,'$. The slight perturbations to the otherwise cylindrical wavefronts is a result of the losses, which degrade the performance of the device by modifying its internal auxiliary reflected fields. For comparison, the fields produced by the lossless implementation of the same design are plotted in Fig. 20 of Appendix C.

It is also worth noting that the presented practical design achieves the desired functionality even without using PMC baffles. This can be attributed to the extremely thin profile of the dielectric substrates [34].

In conclusion, the high-fidelity field transformation realized using coarsely discretized unit cells with realistic lossy meta-atoms hints at the practical viability of more sophisticated cylindrical devices such as the penetrable OBMS cloak.

V. CONCLUSION

We present a mode-matching framework for the analysis and synthesis of scalar cylindrical OBMSs based on the discrete Fourier transform. By decomposing the omega-bianisotropic surface parameters into Fourier harmonics and the electromagnetic fields into cylindrical modes, we transform the bianisotropic sheet transition conditions into simple algebraic equations, which can be solved to either

predict or engineer wave scattering from cylindrical metasurfaces. We also propose a systematic procedure for designing passive and lossless cylindrical OBMSs, which involves enforcement of local power conservation in a straightforward manner. Lastly, to bring these devices one step closer to practical realization, we present methods to realize the derived OBMS surface parameters using a topology consisting of multiple concentric azimuthally varying electric impedance sheets.

We design and investigate several passive and lossless scalar OBMS-based devices including illusion metasurfaces, penetrable metasurface cloaks, and high-gain metasurface antennas. Each device is numerically verified with finite-element simulations, confirming the effectiveness of the proposed method. To demonstrate the practicality of the presented devices, we design an electromagnetic illusion metasurface using realistic PCB-based meta-atoms. Its performance is validated using full-wave simulations.

ACKNOWLEDGMENT

The authors wish to thank Nicolas Faria for the insightful discussions on cylindrical metasurfaces and their applications.

APPENDIX A: ANALYSIS EQUATIONS FOR EXTERNALLY EXCITED CYLINDRICAL OBMSS

The modal transmission matrix $\hat{\mathbf{T}}_{\rm ex}$ and modal reflection matrix $\hat{\mathbf{R}}_{\rm ex}$ for the externally excited TM^z-polarized OBMS pictured in Fig. 5 are as follows:

$$\begin{aligned}
\hat{\mathbf{T}}_{\rm ex} &= \hat{\mathbf{t}}_{{\rm ex},b}^{-1}\hat{\mathbf{t}}_{{\rm ex},a},\\
\hat{\mathbf{t}}_{{\rm ex},a} &= \left(\frac{1}{2}\mathbf{I}+\hat{\mathbf{K}}-\hat{\mathbf{Z}}\mathbf{Y}_{\rm ex}^{r}\right)^{-1}\left(\frac{1}{2}\mathbf{I}+\hat{\mathbf{K}}-\hat{\mathbf{Z}}\mathbf{Y}_{\rm ex}^{i}\right)\\
&\quad-\left(\frac{1}{2}\mathbf{Y}_{\rm ex}^{r}-\hat{\mathbf{Y}}-\hat{\mathbf{K}}\mathbf{Y}_{\rm ex}^{r}\right)^{-1}\left(\frac{1}{2}\mathbf{Y}_{\rm ex}^{i}-\hat{\mathbf{Y}}-\hat{\mathbf{K}}\mathbf{Y}_{\rm ex}^{i}\right),\\
\hat{\mathbf{t}}_{{\rm ex},b} &= \left(\frac{1}{2}\mathbf{Y}_{\rm ex}^{r}-\hat{\mathbf{Y}}-\hat{\mathbf{K}}\mathbf{Y}_{\rm ex}^{r}\right)^{-1}\left(\frac{1}{2}\mathbf{Y}_{\rm ex}^{t}+\hat{\mathbf{Y}}+\hat{\mathbf{K}}\mathbf{Y}_{\rm ex}^{t}\right)\\
&\quad-\left(\frac{1}{2}\mathbf{I}+\hat{\mathbf{K}}-\hat{\mathbf{Z}}\mathbf{Y}_{\rm ex}^{r}\right)^{-1}\left(\frac{1}{2}\mathbf{I}-\hat{\mathbf{K}}+\hat{\mathbf{Z}}\mathbf{Y}_{\rm ex}^{t}\right).
\end{aligned} \tag{A1}$$

TABLE VI. Common geometric parameters (in millimeters) shared among all unit cells in Fig. 18.

Λ_i	Λ_m	Λ_o	h	w	t
4.485	4.523	4.561	10.00	0.132	0.127

TABLE VII. Specific geometric parameters (in millimeters) for the type-A unit cells in Fig. 18.

Cell no.	L_i	L_m	L_o	g_i	g_o
1	2.616	0.508	2.661	1.220	1.336
9, 14	2.616	0.000	2.661	1.220	1.330
10, 13	2.616	0.125	2.661	1.344	1.270
11, 12	2.616	0.168	2.661	1.375	1.230

$$\begin{aligned}
\hat{\mathbf{R}}_{\rm ex} &= \hat{\mathbf{r}}_{{\rm ex},b}^{-1}\hat{\mathbf{r}}_{{\rm ex},a},\\
\hat{\mathbf{r}}_{{\rm ex},a} &= \left(\frac{1}{2}\mathbf{I}-\hat{\mathbf{K}}+\hat{\mathbf{Z}}\mathbf{Y}_{\rm ex}^{t}\right)^{-1}\left(\frac{1}{2}\mathbf{I}+\hat{\mathbf{K}}-\hat{\mathbf{Z}}\mathbf{Y}_{\rm ex}^{i}\right)\\
&\quad-\left(\frac{1}{2}\mathbf{Y}_{\rm ex}^{t}+\hat{\mathbf{Y}}+\hat{\mathbf{K}}\mathbf{Y}_{\rm ex}^{t}\right)^{-1}\left(\frac{1}{2}\mathbf{Y}_{\rm ex}^{i}-\hat{\mathbf{Y}}-\hat{\mathbf{K}}\mathbf{Y}_{\rm ex}^{i}\right),\\
\hat{\mathbf{r}}_{{\rm ex},b} &= \left(\frac{1}{2}\mathbf{Y}_{\rm ex}^{t}+\hat{\mathbf{Y}}+\hat{\mathbf{K}}\mathbf{Y}_{\rm ex}^{t}\right)^{-1}\left(\frac{1}{2}\mathbf{Y}_{\rm ex}^{r}-\hat{\mathbf{Y}}-\hat{\mathbf{K}}\mathbf{Y}_{\rm ex}^{r}\right)\\
&\quad-\left(\frac{1}{2}\mathbf{I}-\hat{\mathbf{K}}+\hat{\mathbf{Z}}\mathbf{Y}_{\rm ex}^{t}\right)^{-1}\left(\frac{1}{2}\mathbf{I}+\hat{\mathbf{K}}-\hat{\mathbf{Z}}\mathbf{Y}_{\rm ex}^{r}\right).
\end{aligned} \tag{A2}$$

To obtain the the modal transmission matrix $\hat{\mathbf{T}}_{\rm PEC}$ and modal reflection matrix $\hat{\mathbf{R}}_{\rm PEC}$, for an OBMS surrounding a PEC cylinder, replace $\mathbf{Y}_{\rm ex}^{\{i,t,r\}}$ with $\mathbf{Y}_{\rm PEC}^{\{i,t,r\}}$.

APPENDIX B: GEOMETRIC PARAMETERS FOR THE PRACTICAL ILLUSION OBMS DESIGN

The 11 unique unit-cell geometries utilized by the design depicted in Fig. 18 are summarized here. The features listed in Table VI are shared among all cells.

The cell-specific parameters are summarized in the following tables, where the cells are grouped into type A (Table VII) and type B (Table VIII) as defined in Sec. IV.

TABLE VIII. Specific geometric parameters (in millimeters) for the type-B unit cells in Fig. 18.

Cell no.	L_i	L_m	L_o	g_i	g_m	g_o	w'
2, 21	2.616	2.638	2.661	1.400	0.262	1.190	0.250
3, 20	2.616	2.638	2.661	1.430	0.380	1.070	0.250
4, 19	2.616	2.427	2.661	2.780	2.000	0.350	0.250
5, 18	2.616	2.638	3.991	1.827	1.680	0.800	0.250
6, 17	2.616	3.958	2.661	1.780	0.000	1.328	0.900
7, 16	2.616	3.958	2.661	1.354	0.000	1.414	0.400
8, 15	2.616	3.958	2.661	1.295	0.000	1.375	0.250

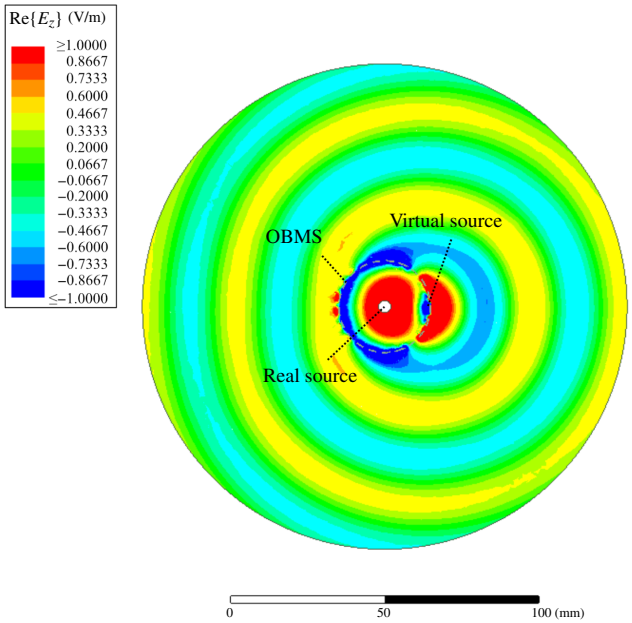

FIG. 20. Simulated Re{E_z} for the practical illusion OBMS design of Fig. 18, neglecting conduction and dielectric losses.

APPENDIX C: SIMULATION RESULTS OF LOSSLESS ILLUSION OBMS

In Fig. 20, we show a snapshot of the simulated electric field distribution for the lossless PCB-based illusion OBMS designed in Sec. IV. As expected, a performance improvement is observed, compared to the results of Fig. 19 which includes non-ideal losses.

[1] Oscar Quevedo-Teruel *et al.*, Roadmap on metasurfaces, J. Opt. **21**, 073002 (2019).

[2] Michael Chen, Minseok Kim, Alex M. H. Wong, and George V. Eleftheriades, Huygens' metasurfaces from microwaves to optics: A review, Nanophotonics **7**, 1207 (2018).

[3] Carl Pfeiffer and Anthony Grbic, Metamaterial Huygens' Surfaces: Tailoring Wave Fronts with Reflectionless Sheets, Phys. Rev. Lett. **110**, 197401 (2013).

[4] V. S. Asadchy, M. Albooyeh, S. N. Tcvetkova, A. Díaz-Rubio, Y. Ra'di, and S. A. Tretyakov, Perfect control of reflection and refraction using spatially dispersive metasurfaces, Phys. Rev. B **94**, 075142 (2016).

[5] G. Xu, S. V. Hum, and G. V. Eleftheriades, Dual-band reflective metagratings with interleaved meta-wires, *IEEE T. Antenn. Propag.* 1 (2020).

[6] Ariel Epstein and George V. Eleftheriades, Synthesis of Passive Lossless Metasurfaces Using Auxiliary Fields for Reflectionless Beam Splitting and Perfect Reflection, Phys. Rev. Lett. **117**, 256103 (2016).

[7] Michael Chen, Elena Abdo-Sánchez, Ariel Epstein, and George V. Eleftheriades, Theory, design, and experimental verification of a reflectionless bianisotropic huygens' metasurface for wide-angle refraction, Phys. Rev. B **97**, 125433 (2018).

[8] M. Chen, A. Epstein, and G. V. Eleftheriades, Design and experimental verification of a passive Huygens' metasurface lens for gain enhancement of frequency-scanning slotted-waveguide antennas, IEEE Trans. Antennas Prop. **67**, 4678 (2019).

[9] G. Xu, S. V. Hum, and G. V. Eleftheriades, A technique for designing multilayer multistopband frequency selective surfaces, IEEE Trans. Antennas Prop. **66**, 780 (2018).

[10] G. Xu, G. V. Eleftheriades, and S. V. Hum, Generalized synthesis technique for high-order low-profile dual-band frequency selective surfaces, IEEE Trans. Antennas Prop. **66**, 6033 (2018).

[11] T. Niemi, A. O. Karilainen, and S. A. Tretyakov, Synthesis of polarization transformers, IEEE Trans. Antennas Prop. **61**, 3102 (2013).

[12] Minseok Kim and George V. Eleftheriades, Design and Experimental Demonstration of Impedance-Matched Circular-Polarization-Selective Surfaces with Spin-Selective Phase Modulations, Phys. Rev. Appl. **13**, 014009 (2020).

[13] M. Selvanayagam and George V. Eleftheriades, Discontinuous electromagnetic fields using orthogonal electric and magnetic currents for wavefront manipulation, Opt. Express **21**, 14409 (2013).

[14] P. Ang and G. V. Eleftheriades, Active cloaking of a non-uniform acatterer, Sci. Rep. **10**, 2021 (2020).

[15] M. Dehmollaian and C. Caloz, in *2019 IEEE International Symposium on Antennas and Propagation USNC/URSI National Radio Science Meeting* (IEEE, Atlanta, GA, USA, 7–12 July, 2019), p. 1323.

[16] Do-Hoon Kwon, Lossless tensor surface electromagnetic cloaking for large objects in free space, Phys. Rev. B **98**, 125137 (2018).

[17] Ariel Epstein and George V. Eleftheriades, Arbitrary power-conserving field transformations with passive lossless omega-type bianisotropic metasurfaces, IEEE Trans. Antennas Prop. **64**, 3880 (2016).

[18] K. Achouri, M. A. Salem, and C. Caloz, General metasurface synthesis based on susceptibility tensors, IEEE Trans. Antennas Prop. **63**, 2977 (2015).

[19] Viktar S. Asadchy, Ana Díaz-Rubio, and Sergei A. Tretyakov, Bianisotropic metasurfaces: Physics and applications, Nanophotonics **7**, 1069 (2018).

[20] Mahdi Safari, Hamidreza Kazemi, Ali Abdolali, Mohammad Albooyeh, and Filippo Capolino, Illusion mechanisms with cylindrical metasurfaces: A general synthesis approach, Phys. Rev. B **100**, 165418 (2019).

[21] Do-Hoon Kwon, Illusion electromagnetics for free-standing objects using passive lossless metasurfaces, Phys. Rev. B **101**, 235135 (2020).

[22] H. Li, C. Ma, F. Shen, K. Xu, D. Ye, J. Huangfu, C. Li, L. Ran, and T. A. Denidni, Wide-angle beam steering based on an active conformal metasurface lens, IEEE Access **7**, 185264 (2019).

[23] M. Dehmollaian, N. Chamanara, and C. Caloz, Wave scattering by a cylindrical metasurface cavity of arbitrary cross

section: Theory and applications, IEEE Trans. Antennas Prop. **67**, 4059 (2019).
[24] S. Sandeep and S. Y. Huang, Simulation of circular cylindrical metasurfaces using GSTC-MoM, IEEE J. Multiscale Multiphys. Comput. Techn. **3**, 185 (2018).
[25] Dominik Barbaric, Zvonimir Sipus, and Zoran Eres, Modeling cascaded cylindrical metasurfaces with spatially-varying impedance distribution, Radioengineering **28**, 505 (2019).
[26] Z. Sipus, M. Bosiljevac, and A. Grbic, Modelling cascaded cylindrical metasurfaces using sheet impedances and a transmission matrix formulation, IET Microw. Antennas Propag. **12**, 1041 (2018).
[27] A. H. Dorrah and G. V. Eleftheriades, Bianisotropic Huygens' metasurface pairs for nonlocal power-conserving wave transformations, IEEE Antennas Wirel. Propag. Lett. **17**, 1788 (2018).
[28] Younes Ra'di and Sergei A. Tretyakov, Balanced and optimal bianisotropic particles: Maximizing power extracted from electromagnetic fields, New J. Phys. **15**, 053008 (2013).
[29] J. P. S. Wong, A. Epstein, and G. V. Eleftheriades, Reflectionless wide-angle refracting metasurfaces, IEEE Antennas Wirel. Propag. Lett. **15**, 1293 (2016).
[30] E. Abdo-Sánchez, M. Chen, A. Epstein, and G. V. Eleftheriades, A leaky-wave antenna with controlled radiation using a bianisotropic Huygens' metasurface, IEEE Trans. Antennas Prop. **67**, 108 (2019).
[31] Gengyu Xu, Sean V. Hum, and George V. Eleftheriades, in *2019 IEEE International Symposium on Antennas and Propagation USNC/URSI National Radio Science Meeting* (IEEE, Atlanta, GA, USA, 7–12 July, 2019), p. 1973.
[32] Junfei Li, Ana Díaz-Rubio, Chen Shen, Zhetao Jia, Sergei Tretyakov, and Steven Cummer, Highly Efficient Generation of Angular Momentum with Cylindrical Bianisotropic Metasurfaces, Phys. Rev. Appl. **11**, 024016 (2019).
[33] Sherman W. Marcus and Ariel Epstein, Fabry-pérot Huygens' metasurfaces: On homogenization of electrically thick composites, Phys. Rev. B **100**, 115144 (2019).
[34] G. Xu, Sean V. Hum, and George V. Eleftheriades, Augmented Huygens' metasurfaces employing baffles for precise control of wave transformations, IEEE Trans. Antennas Prop. **67**, 6935 (2019).
[35] Jianjia Yi, Paul-Henri Tichit, Shah Nawaz Burokur, and André de Lustrac, Illusion optics: Optically transforming the nature and the location of electromagnetic emissions, J. Appl. Phys. **117**, 084903 (2015).
[36] Constantine A. Balanis, *Advanced Engineering Electromagnetics* (John Wiley & Sons, Inc., New Jersey, 2012), 2nd ed.
[37] M. Selvanayagam and G. V. Eleftheriades, An active electromagnetic cloak using the equivalence principle, IEEE Antennas Wirel. Propag. Lett. **11**, 1226 (2012).
[38] D. Schurig, J. J. Mock, B. J. Justice, S. A. Cummer, J. B. Pendry, A. F. Starr, and D. R. Smith, Metamaterial electromagnetic cloak at microwave frequencies, Science **314**, 977 (2006).
[39] Zhi Hao Jiang, Peter E. Sieber, Lei Kang, and Douglas H. Werner, Restoring intrinsic properties of electromagnetic radiators using ultralightweight integrated metasurface cloaks, Adv. Funct. Mater. **25**, 4708 (2015).
[40] Ariel Epstein, Joseph Wong, and George V. Eleftheriades, Cavity-excited Huygens' metasurface antennas for near-unity aperture illumination efficiency from arbitrarily large apertures, Nat. Commun. **7**, 10360 (2016).